

**ADVERTIMENT.** La consulta d'aquesta tesi queda condicionada a l'acceptació de les següents condicions d'ús: La difusió d'aquesta tesi per mitjà del servei TDX ([www.tesisenxarxa.net](http://www.tesisenxarxa.net)) ha estat autoritzada pels titulars dels drets de propietat intel·lectual únicament per a usos privats emmarcats en activitats d'investigació i docència. No s'autoritza la seva reproducció amb finalitats de lucre ni la seva difusió i posada a disposició des d'un lloc aliè al servei TDX. No s'autoritza la presentació del seu contingut en una finestra o marc aliè a TDX (framing). Aquesta reserva de drets afecta tant al resum de presentació de la tesi com als seus continguts. En la utilització o cita de parts de la tesi és obligat indicar el nom de la persona autora.

**ADVERTENCIA.** La consulta de esta tesis queda condicionada a la aceptación de las siguientes condiciones de uso: La difusión de esta tesis por medio del servicio TDR ([www.tesisenred.net](http://www.tesisenred.net)) ha sido autorizada por los titulares de los derechos de propiedad intelectual únicamente para usos privados enmarcados en actividades de investigación y docencia. No se autoriza su reproducción con finalidades de lucro ni su difusión y puesta a disposición desde un sitio ajeno al servicio TDR. No se autoriza la presentación de su contenido en una ventana o marco ajeno a TDR (framing). Esta reserva de derechos afecta tanto al resumen de presentación de la tesis como a sus contenidos. En la utilización o cita de partes de la tesis es obligado indicar el nombre de la persona autora.

**WARNING.** On having consulted this thesis you're accepting the following use conditions: Spreading this thesis by the TDX ([www.tesisenxarxa.net](http://www.tesisenxarxa.net)) service has been authorized by the titular of the intellectual property rights only for private uses placed in investigation and teaching activities. Reproduction with lucrative aims is not authorized neither its spreading and availability from a site foreign to the TDX service. Introducing its content in a window or frame foreign to the TDX service is not authorized (framing). This rights affect to the presentation summary of the thesis as well as to its contents. In the using or citation of parts of the thesis it's obliged to indicate the name of the author

Doctoral Thesis

NUMERICAL ANALYSIS  
OF CONCRETE-FILLED TUBES WITH STIFFENING PLATES  
UNDER LARGE DEFORMATION AXIAL LOADING

phD student  
Albert Albareda Valls

Directed by  
Dr. Jordi Maristany Carreras

June 2012

## Chapter IV

### CONSIDERATIONS ABOUT THE NUMERICAL ANALYSIS

\*\*\*

Chapter IV pretends to resume and expose all the considerations assumed for the numerical model which have been progressively validated during the progress of this investigation.

Main efforts during this research have been focused on obtaining a reliable FE model, capable of reproducing the structural behavior of CFT sections. This objective involves the use of a complex constitutive material model for concrete which could simulate the compressive response of concrete subjected to high hydrostatic pressures.

Thus, after describing the different families of models which have been developed, this Chapter provides a detailed explanation about general features of them. After this, a specific description of the process of calibration of the geometrical and material features of the model is presented in Sections 4.4 and 4.5.

The purpose of this Chapter, apart from providing to future researchers the tools necessary to be capable of modeling concrete-filled tubes and composite sections in general, is to reflect the work done in terms of calibrating the numerical models and to justify the validity of the results.

\*\*\*

## **Chapter IV**

# **CONSIDERATIONS ABOUT THE NUMERICAL ANALYSIS**

### **4.1 The simulation method.**

- 4.1.1 The finite element method.
- 4.1.2 Software used in the analysis.

### **4.2 Models proposed in this investigation.**

- 4.2.1 Preliminary elastic models to check geometry.
- 4.2.2 Models used to calibrate material nonlinearities.
- 4.2.3 Models used to compare FE results with experimental tests.
- 4.2.4 Definitive models.

### **4.3 General features of the models.**

- 4.3.1 Explicit formulation for dynamic analyses.
- 4.3.2 Element types used in the analysis.
  - 4.3.2.1 Element types used in models done by ANSYS.
  - 4.3.2.2 Element types used in models done by ABAQUS.

### **4.4 Calibration of material models used in the analysis.**

- 4.4.1 Material model used for steel.
  - 4.4.1.1 General parameters adopted for steel.
  - 4.4.1.2 Plasticity model used for steel.
- 4.4.2 Material models used for concrete.
  - 4.4.2.1 General parameters adopted for concrete.
  - 4.4.2.2 Previous considerations and preliminary models.
  - 4.4.2.3 Elastic perfectly-plastic model with tension cutoff for concrete.
  - 4.4.2.4 Damaged Plasticity Model for concrete [DPM]
- 4.4.3 Contact model to reproduce the interaction between the two components.
  - 4.4.3.1 Normal contact.
  - 4.4.3.1 Tangential contact.

### **4.5 Calibration of geometrical features of the models.**

- 4.5.1 Calibration of the mesh size.
- 4.5.2 Calibration of boundary conditions.
- 4.5.3 Calibration of the domain of the model.
  - 4.5.3.1 Calibration of the size of the specimen.
  - 4.5.3.2 Calibration of the symmetry condition.
- 4.5.4 Calibration of the loading conditions.



#### 4.1 The simulation method.

This investigation has been carried out by means of numerical analyses only. Thus, the need of calibrating the proposed models with real experimental tests has been assumed as necessary. However, an experimental campaign is also proposed as a further objective in order to compare and validate the results obtained in this investigation.

##### 4.1.1 The finite element method [FEM].

The method of analysis used in this work is the FEM [Finite Element Method]. This methodology of analysis uses numerical formulations to approximate real behaviors. It is important to remember that this method provides only an approximation to real problems; therefore, the obtained results come from a simulation of material behaviors, and not from reality. Due to complexity of the method and the sensibility of the results to the input data, it is strictly necessary to carry out a preliminary process of calibration of the models.

The FE method is the most powerful tool nowadays in order to analyze the behavior of structural elements or physical environments by means of simulation. With this purpose, a FE analysis requires an accurate discretization of the reality: this means a simplification of geometries and shapes into more or less dense meshes, formed by three-dimensional prismatic or tetrahedral elements. Each one of these elements disposes of a specific number of nodes, all them implemented in the general formulation of the problem, from which we are capable of obtaining the value of the resulting forces and displacements.

With the aim of approximating the results to reality as maximum as possible, and in order to give veracity to the conclusions of this work, the calibration process of geometry and constitutive models is accurately described in this Chapter. All the variables which can have a direct effect on results have been analyzed in the following Sections, such as: the definition of the constitutive models for materials, the mesh size, the global size of specimens and the boundary conditions.

##### 4.1.2 Software used in the analysis.

The software used is basically ANSYS, version 11, and ABAQUS version 6.10. During the initiation in modeling, the preliminary analyses were carried out in ANSYS, while the last ones have been done in ABAQUS, thanks to the possibilities of the model available for concrete in the latter<sup>1</sup>. However, both commercial products solve professionally any constitutive behavior. As it will be explained in further Sections, the fact of initiating the investigation with simple models in ANSYS has been extremely useful for this investigation. Previous analyses using elastic perfectly-plastic models for concrete have been done necessarily to understand the others. These models have become decisive in order to reproduce and comprehend the behavior of confined concrete, as they have provided not only conclusions to this Thesis, but also a different point of view to the final proposed models.

Although any steel-concrete composite section can be modeled using ANSYS, it is really useful to dispose a constitutive material model for concrete that could take also the evolution of damage into account. ANSYS disposes of the element type SOLID65, which combined with the material model “concrete” is capable of reproducing the failure surface of the material by defining a *crushing* and *cracking* criteria<sup>2</sup>. However, the use of this constitutive model requires a complex calibration of nine different variables in order to define the mentioned yield surface, combined with the failure

---

<sup>1</sup> See Section 4.4.2.4

<sup>2</sup> See Section 4.4.2.2

surface simultaneously. This can be relatively simple in case of flexural or tensile states –like for beam elements. Otherwise, the calibration of these variables may become really complex under states of large deformation axial loading. In this case, the difficulty will lie in matching the yield surface with the failure surface under compression, assuming that any small variation of the input data could vary their shape significantly. In addition, the lack of a damage evolutionary criterion in the “concrete” model of ANSYS leads directly to a bad reproduction of the post-*peak*<sup>3</sup> behavior.

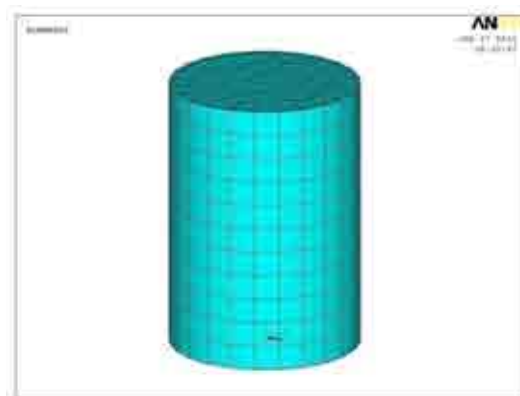
Contrarily, ABAQUS disposes of another complex material model for concrete: “*Damaged Plasticity for Concrete*”, which allows reproducing with accurate precision the degradation process of concrete under compression [*crushing*] and the confinement effect under high hydrostatic states<sup>4</sup>. This model gives the possibility of reproducing the behavior of concrete much more precisely than the mentioned model “concrete” of ANSYS. This is the reason why this work has combined the two models, by using preferably the latter.

#### 4.2 Models proposed in this investigation.

In the course of this investigation, and with the final purpose of obtaining results capable of giving reliable arguments to the initial hypothesis, different families of models have been done, depending on their finality, complexity and available processing hardware.

##### 4.2.1 Preliminary elastic models to check geometry.

Previous to the definitive models for the final analysis, a set of different tests have been carried out in order to calibrate the behavior of confined concrete, really different from that under other states. These models have been also used to reproduce the interaction between both materials. The calibration of these starting models has employed the same time as the used for acquiring a minimum theoretical background about CFT behavior; it is really important that this process goes hand in hand in order to well understand the simulation used. A wrong definition of the input data would lead to a lack of contact between the two components involved, directly.



**Fig. IV.1. First elastic models done in ANSYS.**

They have been used to verify the geometry and contact.

As it has been explained before, the first models were done in ANSYS –strictly in the elastic range, with the objective of detecting all the possible problems related with geometry and contact behavior. In these first models, only concrete was loaded to guarantee a correct bond between the

<sup>3</sup> *Peak of load*: Point of the load-strain diagram corresponding to the load-bearing capacity.

<sup>4</sup> See Section 4.4.2.4

two materials, thanks to its volumetric expansion. These models only worked with the assumption of this hypothesis, since while the elastic Poisson's ratio for concrete ranges from 0.15 to 0.18, the corresponding value for steel is about 0.29. This fact implies that, in case of considering both components loaded together, the transversal deformation of the tube was always larger than the lateral expansion of the core; therefore, in this case the contact between them never appeared.

This phenomenon can be easily justified through the following expression for lateral strain of a circular ring in the elastic range [see figure IV.2]:

$$\varepsilon_{trans} = \varepsilon_{long} \cdot \nu \quad (4.1)$$

$$\text{If } \varepsilon_{trans} = \frac{\Delta R}{R} \text{ being } \varepsilon_{long} = \frac{\Delta L}{L}, \text{ then:} \quad (4.2)$$

$$\frac{\Delta R}{R} = \frac{\Delta L}{L} \cdot \nu \quad (4.3)$$

And, as a consequence:

$$\Delta R = \frac{\Delta L \cdot R}{L} \cdot \nu \quad (4.4)$$

being  $L$ , the column length and  $R$ , the radius of the section.

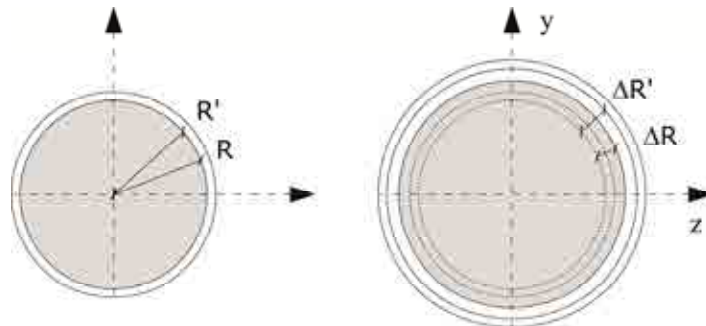
Therefore, being the radius and the length equivalent, the largest transversal strain appears in the component with the largest elastic Poisson's coefficient,  $\nu$  [in this case the steel, with a value of 0.29]. Even in further models where perfect-plasticity has been assumed, the Poisson's ratio reached values of 0.49 in the two components simultaneously due to the plastic behavior of materials. However, lateral strains did not go beyond, as dilatancy was not considered.

Then, in these preliminary models, the following condition was imposed:

$$\text{if } \nu_a > \nu_c \rightarrow \Delta R' > \Delta R \quad (4.5)$$

being:

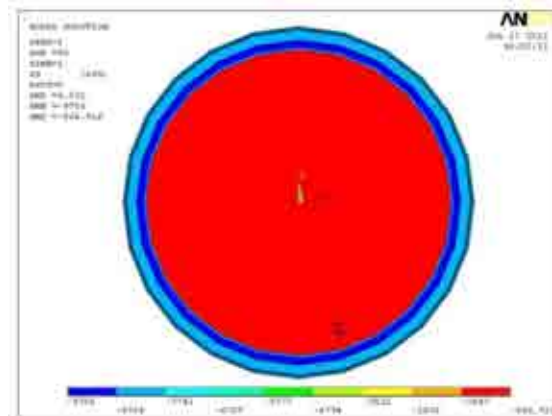
$\nu_a$	Poisson's ratio of steel
$\nu_c$	Poisson's ratio of concrete.
$R'$	Inner radius of the steel tube.
$R$	Radius of the concrete core.



**Fig. IV.2. Mode of transversal deformation of the two components in the elastic range.**

Assuming  $\nu_a = 0.29$  and  $\nu_c = 0.18$ , the contact between the two surfaces did never occur.

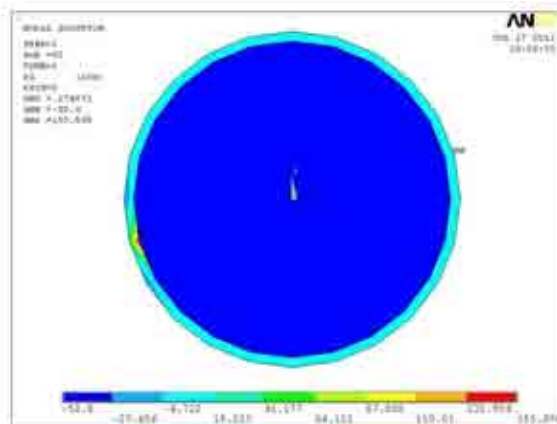
$R'$  is the inner radius of the steel tube, and  $R$  the radius of the core; thus:  $R' = R$ .



**Fig. IV.3. Image of the existing gap between the two components.**

Results obtained from a preliminary elastic model, where the two components were simultaneously loaded.

In figures IV.2 and IV.3, it can be noted how the two components never were in contact, so that the steel tube did not achieve to confine the core. This effect was caused by loading both components at the same time, and due to having defined the materials so that they were governed by their respective Poisson's ratios only. As it has been explained before, really different was the response of the section by loading only concrete: under this assumption, only the core expanded transversally, guaranteeing this way full contact in the interface.



**Fig. IV.4. Image of the two components fully in contact, thanks to loading only the core.**

In this case, both components got in contact as the unique one which really expanded laterally was the core, independently of the Poisson's coefficients of both materials.

The purpose of these preliminary models was to calibrate the geometry and the behavior of contact elements, in order to assure the numerical convergence before considering the full complexity of the material nonlinearities. It is important to point out that contact elements in the models imply automatically nonlinearities in the process. If the problem involves also geometrical or material nonlinearities, the achievement of numerical convergence may be a slow and gradual process, full of complexity.

Once the model had enough numerical sturdiness [considering that the model and contact elements worked well assumed elastic], the following step in the process was to introduce the material

nonlinearities. The preliminary nonlinear constitutive models for steel and concrete are described in Sections 4.4.1 and 4.4.2.2 of this Chapter. The solution to the problem of volumetric expansion of concrete and the appearance of confinement effect is more complex than assuming only a yield criterion for concrete, as it can be derived from the following Sections.

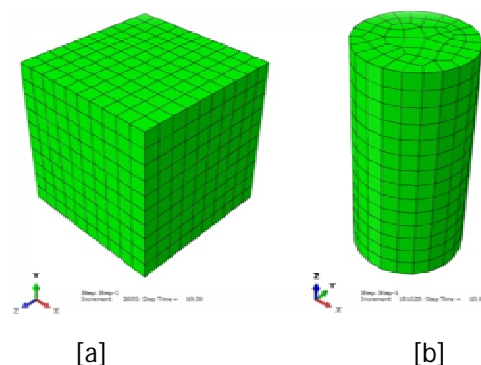
The major challenge in modeling has been to achieve a correct reproduction of the confinement effect of concrete by means of controlling the transversal expansion in both materials; this effect has to be calibrated through choosing the most suitable yield criterion for both cases, as it will be shown later.

#### 4.2.2 Models used to calibrate material nonlinearities.

With the objective of verifying the constitutive material models used in this investigation, specific models for validation purpose have been done. The input data used to determine the constitutive models have been calibrated independently, according to literature.

The calibration of the model considered for steel is definitively much simpler than the model for concrete, since it is really well-described by literature and it does not show important variations. Its similar response under tension as well as compression, and its yielding behavior defined by a perfect-plasticity criterion<sup>5</sup> lead to a model controlled by few variables. The calibration has been done by using a cylindrical specimen of 150 mm width and 300 mm height, with the two bases restricted against rotation and deformation [Fig. IV.5]. These analyses have been done under pure tension and pure compression states, up to the collapse in all cases. Only steels S275 and S355 have been used.

Contrarily, the calibration of concrete is really more complex than in case of steel, being really crucial due to the intrinsic complexity of its behavior. Final results of this work depend on the accuracy of the material model used for concrete directly. Since two constitutive models have been used for concrete in this investigation<sup>6</sup>, the calibration has been done for the two, and especially for those situations involving high hydrostatic pressures [apart from uniaxial and biaxial states]. In order to compare the results obtained from calibration with those coming from experimental tests and literature, a cubic specimen of 150 mm width has been used.



**Fig. IV.5. Specimens used for the calibration of material models.**  
Specimen for concrete [a] and specimen for steel [b].

<sup>5</sup> See Section 4.4.2.3

<sup>6</sup> See Section 4.4.2

To calibrate the curves obtained from this verification, the expression (2.71) proposed by del Viso and Carmona<sup>7</sup> (Viso, et al., 2008) has been used. This expression is useful for determining the correspondence between cylindrical and cubic specimens, as the compressive strength of concrete always refers to the cylindrical samples.

As it will be explained in Section 4.4.2, the two constitutive models used in this investigation have been verified by using the two different available numerical tools, ANSYS and ABAQUS. On the one hand, the increment of compressive strength under different hydrostatic states has been analyzed and on the other hand, those parameters which govern dilatancy in plasticity have been also calibrated; parameters which furthermore become crucial, assuming that transversal strains are decisive to determine the confinement effect.

#### **4.2.3 Models used to compare the FE results with experimental tests.**

Once the specimens used to calibrate the constitutive models for steel and concrete were accepted, a set of different specimens were also analyzed in order to compare the FE results with those obtained from experimental tests [assuming the same conditions as in the experiments]. These models were made by using the verified geometry and the constitutive material models, previously calibrated. The FE simulation of the experimental tests has been done by following the same boundary and loading conditions exactly, in order to obtain the most accurate results as possible. This was the last step before facing the complete analysis, being strictly necessary in a numerical investigation; the importance of this phase is especially decisive in this work, since final conclusions not only depend on the behavior of the two materials, but also on the interaction between them. For verification purpose, eight different specimens with different D/t ratios and different material strengths have been modeled: four circular and four square-shaped CFT sections, according to those used by Susantha together with Ge (Susanta, et al., 2000)<sup>8</sup>. Obtained results have been compared with those coming from experimental tests [Fig. IV.6].

As it will be explained in further Sections, the main objective of these analyses is to determine the accuracy of the FE curves compared with the experimental tests, especially in the *post-peak* period up to strains of 4%-5%. Both confinement and softening periods have been calibrated using these eight different specimens, tested before by several researchers. However, one extra section [this time, CFDST<sup>9</sup>] has also been modeled in order to calibrate not only the softening behavior, but also the large deformation axial loading response [for strains up to 25%]. These calibration has been done according to the experimental tests carried out by Zhao (Zhao, et al., 2010) [see Chapter V].

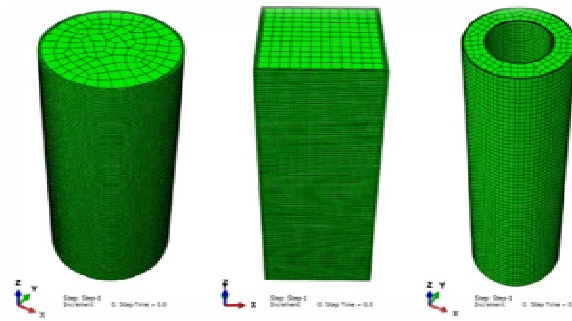
Besides, most of these analyses have been done by following the two different constitutive models mentioned for concrete, and using the two different commercial products, ANSYS and ABAQUS. These models have been also very useful for determining important factors, such as the definitive mesh size or the global domain of the models; all the results of these analyses are shown in the first Section of Chapter V.

---

<sup>7</sup> See Section 2.2.8.1

<sup>8</sup> See Chapter V.

<sup>9</sup> CFDST: Concrete-filled Double Skin Tube Section



**Fig. IV.6. Different examples of the models used for verifying the FE results with real tests.**

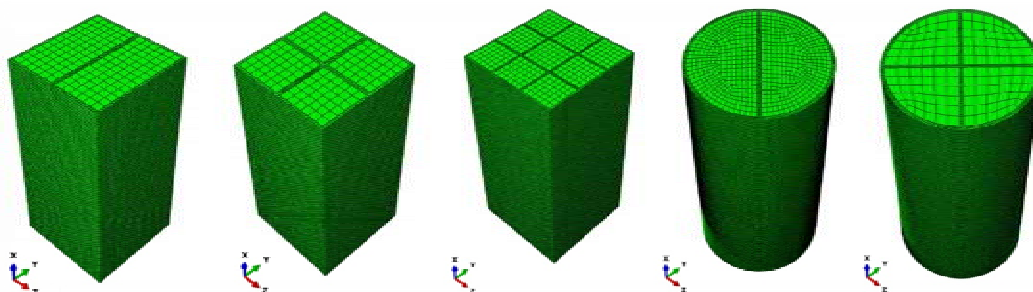
All they have been strictly modeled by following the real conditions of the tests.

#### 4.2.4 Definitive models.

Finally, and after having calibrated the preliminary models up to matching the FE curves with the experimental ones, the definitive models have been done in order to obtain final conclusions of this investigation. Although more than 30 different specimens have been solved, with different  $D/t$  ratios and different material strengths, the analysis which has been carried out in this investigation pretends to be more a descriptive study than a parametric analysis, owing to the complexity of the models and the processing requirements. As it will be explained in Chapter VI, five different reticulated typologies have been analyzed: R2, R4, R9, C2 and C4, depending on the shape of the outer tube and the number of inner cells [see Fig. IV.7]. Two families of specimens [of 5 mm and 10 mm of outer wall-thickness] belonging to each different typology have been analyzed, by changing the strength of the concrete filling [ranging from 30 to 50MPa], [see Chapter VI].

Ten more extra CFT sections have been also analyzed, equivalent in area of steel and concrete, but without stiffening plates. Main objective of analyzing these 10 equivalent sections, two specimens corresponding to each typology by couples of 5 and 10 mm plate thickness, is to determine the gain in strength and ductility provided by stiffening circular and square CFT sections.

These models and their derived conclusions constitute the main body of this investigation; owing to the required complexity and precision, these models have been developed entirely in ABAQUS software, assuming that the material model "*Concrete Damaged Plasticity*" available in this software is the most suitable to reproduce the behavior of the concrete filling in CFT sections.



**Fig. IV.7. Models of the definitive typologies analyzed**

A total of 40 different specimens have been analyzed.

### 4.3 General features of the models.

The models proposed in this research show a combination of three different nonlinearities: those coming from the constitutive material models, those coming from geometry [local buckling] and finally, those coming from contact elements. In order to solve faithfully the problem, two different formulations have been used: on the one hand, preliminary models were analyzed using a static analysis based on the Newton-Rapshon algorithm. This formulation solves faithfully any kind of geometrical or material nonlinear problem, but it implies an important effort in defining the loading step size to manage the convergence of the problem. In case of having a large amount of nodes and elements subjected to geometrical nonlinearities and contact surfaces, this procedure becomes quite impractical. For this reason, the definitive models have been processed by using an explicit dynamic formulation, although the problems proposed are actually, static. Then, this methodology can be summarized in solving static problems by using dynamic formulations: the equation that governs displacements in this case is a second-order differential equation, which represents the natural equilibrium of elastic forces, damping forces and inertial forces.

#### 4.3.1 Explicit formulation for dynamic analyses.

As it has been mentioned in the previous paragraph, the explicit formulation uses dynamic concepts such as velocity and acceleration, but it can also be used to solve static problems. The equations of motion for the body are integrated using the explicit central difference integration rule:

$$\dot{u}^{(i+\frac{1}{2})} = \dot{u}^{(i+\frac{1}{2})} + \frac{\Delta t^{(i+1)} + \Delta t^{(i)}}{2} \ddot{u}^{(i)} \quad (4.6)$$

$$u^{(i+1)} = u^{(i)} + \Delta t^{(i+1)} \dot{u}^{(i+\frac{1}{2})} \quad (4.7)$$

Being  $u$  the displacement,  $\dot{u}$  the velocity and  $\ddot{u}$  the acceleration. The subscript  $(i)$  refers to the increment number, and  $(i + 1/2)$  and  $(i - 1/2)$  refer to midincrement values. The central difference integration operator is explicit in that the kinematic can be advanced using known values of  $\dot{u}^{(i-1/2)}$  and  $\ddot{u}^{(i)}$  from the previous increment. The explicit integration rule is simple but by itself does not provide the computational efficiency associated with the explicit dynamics procedure. The key to the computational efficiency of the explicit procedure is the use of diagonal element mass matrices, as the inversion of the mass matrix that is used in the computation for the accelerations at the beginning of the increment is triaxial:

$$\ddot{u}^{(i)} = M^{-1} \cdot (F^{(i)} - I^{(i)}) \quad (4.8)$$

where  $M$  is the diagonal lumped mass matrix,  $F$  is the applied load vector, and  $I$  is the internal force vector. The explicit procedure requires no iterations and no tangent stiffness matrix.

Special treatment of the mean velocities  $\dot{u}^{(i+\frac{1}{2})}$ ,  $\dot{u}^{(i-\frac{1}{2})}$  etc. is required for initial conditions, certain constraints, and results. For presentation of results, the state velocities are stored as a linear interpolation of the mean velocities:

$$u^{(i+1)} = \dot{u}^{(i+\frac{1}{2})} + \frac{1}{2} \Delta t^{(i+1)} \ddot{u}^{(i+1)} \quad (4.9)$$



The central difference operator is not self-starting because the value of the mean velocity  $\dot{u}^{(i-\frac{1}{2})}$  needs to be defined. The initial values (at time  $t = 0$ ) of velocity and acceleration are set to zero, unless they are previously specified. The following condition can be asserted:

$$\dot{u}^{(+\frac{1}{2})} = \dot{u}^{(0)} + \frac{\Delta t^{(1)}}{2} \ddot{u}^{(0)} \quad (4.10)$$

And finally, the substitution of this expression into the update expression for  $\dot{u}^{(i+\frac{1}{2})}$  yields the following definition of  $\dot{u}^{(-\frac{1}{2})}$ :

$$\dot{u}^{(-\frac{1}{2})} = \dot{u}^{(0)} - \frac{\Delta t^{(0)}}{2} \ddot{u}^{(0)} \quad (4.11)$$

### 4.3.2 Element types used in the analysis.

Element types in a FE analysis define the typology of the problem. The elements used in this investigation have been chosen according to the material nonlinearities, the complexity of the geometry and the requirements needed by the analysis. It is very important to do a good election of the element type for each component, in order to obtain the most accurate results as possible and also to avoid distortions. Since each commercial software product disposes a different collection of element types, the elements used in this work for each case are mentioned in the following two Sections.

#### 4.3.2.1 Element types used in models done by ANSYS.

In models done by ANSYS software, the element type SOLID65 for concrete and the element type SHELL181 for steel have been chosen, according to literature (Malone, 1998), (Kachlakev, 2001); besides, two other additional contact types have been also implemented in the analysis: TARGE170 and CONTA174, according to (Ferrer Ballester, 2005).

The well-known element SOLID65 -widely used and commented in literature-, is a solid and three-dimensional element of eight nodes and three degrees of freedom. It works with those constitutive models specific for concrete, and also available in ANSYS, such as DP+CONC or MISO+CONC<sup>10</sup>. This element type allows considering *cracking* and *crushing* features as well as other characteristic behaviors of concrete such as creep, by using the specific constitutive model known as “concrete” [Fig. IV.8].

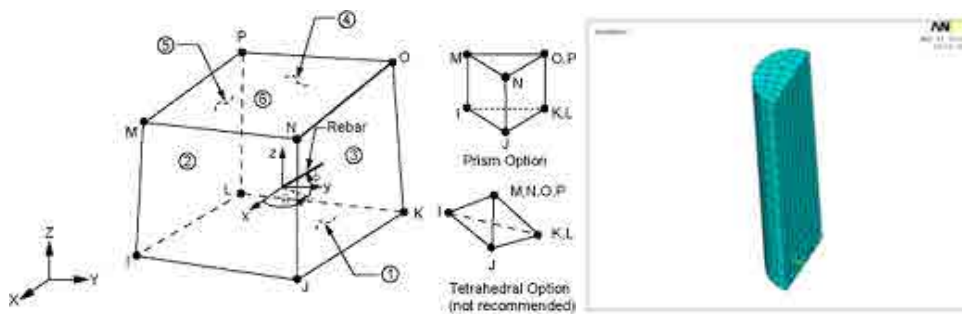
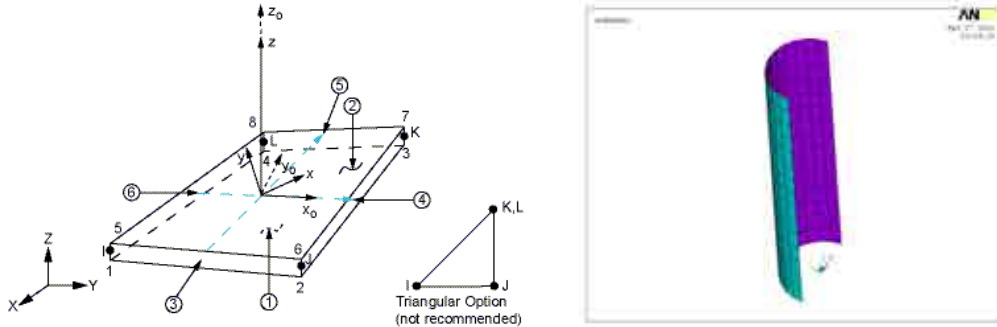


Fig. IV.8. Element type SOLID65 for concrete core.

<sup>10</sup> See Sections 4.4.2.2 and 4.4.2.3

It is a three-dimensional brick element with eight nodes and three degrees of freedom.

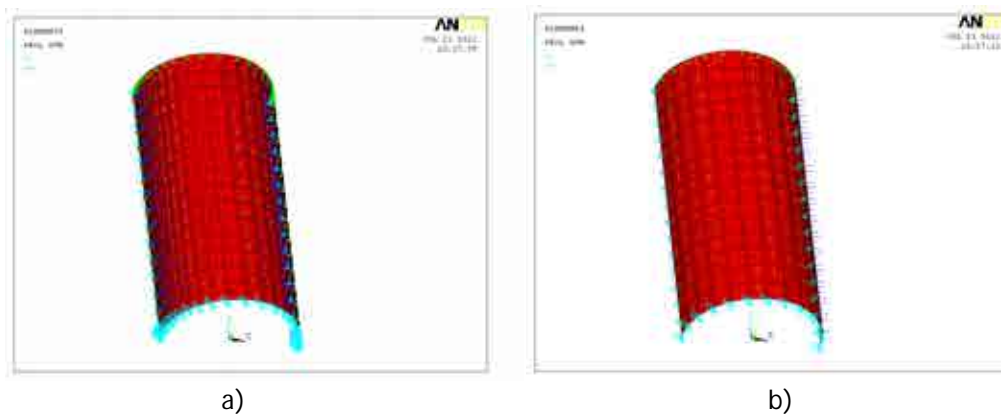
For modeling steel plates and shells, the element type SHELL181 is commonly used; this ET<sup>11</sup> is a four-node element, with six degrees of freedom at each node. It is suitable for problems involving large deformations and plasticity behaviors, and it considers the change in the wall-thickness during the loading process [Fig. IV.9].



**Fig. IV.9. Element type SHELL181 for the steel tube.**

It is a three-dimensional shell element with four nodes and six degrees of freedom.

Finally, for contact surfaces, the elements TARGE170 and CONTA174 have been used for the *target* [sliding object] and the *contact* [surface where the target slides on], respectively [Fig. IV.10]. These two elements allow the possibility of defining intermediate nodes [second order surfaces] and analyses involving large deformations. Besides, they do not have geometric restrictions [in the case of this investigation, they work perfectly for cylindrical surfaces] and require a few number of elements -a fact that reduces notably the processing requirements.



**Fig. IV.10 Element types TARGE170 (a) and CONTA174 (b)**

The first is used for the sliding object [steel tube], while the latter is used for the target surface [concrete core].

It is important to point out that the election of the *target* and the *object* in each case is very important to guarantee the accuracy of the obtained results. For the case proposed in this investigation, the *target* corresponds to the steel tube [the sliding component] while the *object* coincides with concrete core [the supporting component]. It is important to define accurately the normal directions of each contact element in every different case, one opposite to the other. In case of not matching these axes, the contact does not behave properly.

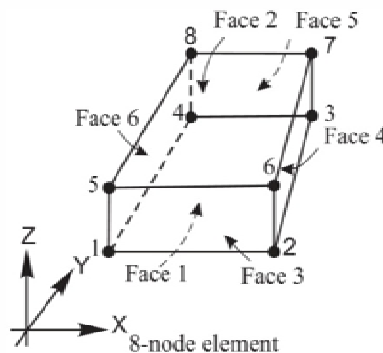
<sup>11</sup> Element Type

#### 4.3.2.2 Element types used in models done by ABAQUS.

A unique three-dimensional brick element, called C3D8, has been used for those models done by ABAQUS. Both components -steel and concrete- have been modeled using the same element in order to get more realistic simulations, and to obtain more expressive deformed shapes. Although it would have been also possible to consider shell elements such as S4R for the steel tube (Xiong, et al., 2007), the fact of modeling also the tubes with solid elements allow a clearer representation of local buckling and, therefore, the mode of collapse. This criterion has been chosen thanks to the available processing hardware and the numerical possibilities of the element C3D8, a product by Simulia© [C3D8 is prepared for three-dimensional problems, involving plasticity behaviors and large strains]. However, it is true that the fact of modeling a plate with solid elements [more similar to a "shell" than to a "solid"] requires really fine meshes, with two or more elements in the wall-thickness at least<sup>12</sup>, in order to consider the stress variations across the wall-thickness.

To finally decide the appropriate element types for each component, some existing literature devoted to similar numerical analyses about CFT sections has been used, such as the study carried out by Starossek and his collaborators (Starossek, et al., 2008).

As it has been already mentioned, element C3D8 is a three-dimensional brick element of eight nodes and three degrees of freedom at each node [Fig. IV.11]. This element is suitable for linear analyses and also for more complex nonlinear processes involving contacts, plasticity and large deformations. The reduced integration is not convenient in this analysis, since the detection of the variations of stress across the wall-thickness becomes crucial during local buckling; in case of using element types with reduced integration [in this case would be C3D8R], the measurement of stress would be reduced into one point per element.



**Fig. IV.11 Element type C3D8 used for concrete core and steel tube.**

It is a three-dimensional element of eight nodes and three degrees of freedom.

It is important to point out that, apart from the qualities mentioned before about the element C3D8, this element also shows a notable capacity of remaining undistorted; this is one of the reasons why the size of the meshes proposed is relatively fine, compared with the global size of the specimens tested [see Section 4.6.1]. The three degrees of freedom at each node of the element C3D8, are the ones corresponding to a three-dimensional solid;  $u, v, w$ , and its resulting stresses are  $S11$  [ $\sigma_{11}$ ; principal normal stress 11],  $S22$  [ $\sigma_{22}$ ; lateral normal stress 22],  $S33$  [ $\sigma_{33}$ ; lateral normal stress 33],  $S12$  [ $\tau_{12}$ ; tangential stress 12],  $S23$  [ $\tau_{23}$ ; tangential stress 23] y  $S13$  [ $\tau_{13}$ ; tangential stress 13].

<sup>12</sup> see Section 4.6.1

#### 4.4 Material models used in the analysis.

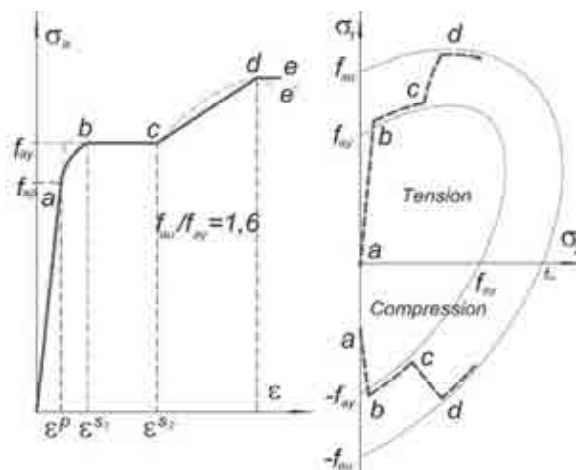
Different material behaviors have been defined for the analysis carried out in this work. Nonlinear models have been proposed for both the steel and concrete, with different plasticity criteria for each material, according to the final purpose of the models.

##### 4.4.1 Material model used for steel.

Steel is an isotropic material, characterized by having an extended elastic range and with an important ductility before the failure [See Section 2.1]. In an advanced plastic strain range after yielding, the material shows a hardening phase by reaching stresses up to 40% higher than its yield limit stress. Its plastic behavior can be perfectly defined through the von Mises yield criterion and its cylindrical surface [see Section 2.1.4], with an important growth during the hardening period from  $f_y$  to  $1.40f_y$ <sup>13</sup>.

##### 4.4.1.1 General parameters adopted for steel.

The representing values for the stress-strain curve of steel have been adopted from literature. The uniaxial stress-strain curve for structural steel has been studied by several researchers in the past, being nowadays really well-known by the engineering community<sup>14</sup>.



**Fig. IV.12 Idealized stress-strain curve for steel.**

(Kuranovas, et al., 2009)

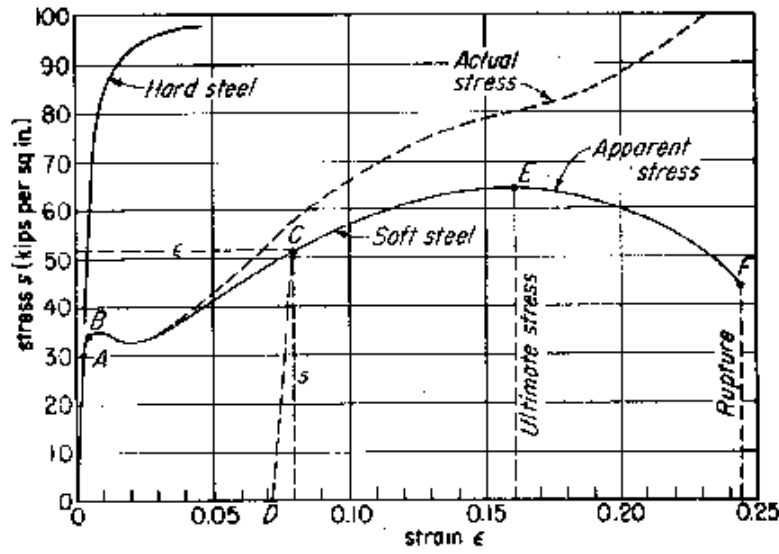
The values for the common mechanical parameters [such as the Young Modulus and the Poisson's ratio in the first elastic range, up to point **b** of figure IV.12], are the parameters mentioned in expressions (2.1) and (2.2) of Section 2.1.1: 210000 MPa for the Young Modulus and 0.283 for the elastic Poisson's ratio.

In reference to the uniaxial stress-strain diagram, it is important to point out that for large deformation axial loading analyses of ductile materials, it is crucial to consider the true stress-strain curve instead of the usual engineering one. The true stress-strain curve takes a slightly

<sup>13</sup> Being  $f_y$  the yield limit stress.

<sup>14</sup> See Section 2.1.4

different form, and it is also known as the “*actual or natural stress curve*” in figure IV.13. For strains over 2.5%, the stress tends to grow up indefinitely with no descent:



**Fig. IV.13 Comparison between the actual [true] and the apparent [engineering] stress-strain curves for structural steel.**

Important variation is observed in advanced strain ranges [curves for uniaxial tension].

This difference is caused by the important reduction [or increment] of transversal area that the tested specimen shows, subjected to large deformation axial loading and owing to the effect of its Poisson's coefficient [see Fig. IV.14]. Usually, strain from a uniaxial compressive or tensile test can be calculated through:

$$\varepsilon = \frac{L_{\text{deformed}} - L_{\text{initial}}}{L_{\text{initial}}} \quad (4.12)$$

being:

$$\begin{array}{ll} L_{\text{deformed}} & \text{Length of the deformed specimen.} \\ L_{\text{initial}} & \text{Original length of the undeformed specimen.} \end{array}$$

By dividing the deformation in infinitesimal increments,  $dL$ , then we get the true strain:

$$d\varepsilon = \frac{dL}{L} \quad (4.13)$$

And the total true strain for a change of the gauge length from  $L_{\text{initial}}$  to  $L_{\text{deformed}}$  is:

$$\varepsilon = \int_0^{\varepsilon} d\varepsilon = \ln \frac{L_{\text{deformed}}}{L_{\text{initial}}} \quad (4.14)$$

This last expression defines the true strain, and takes also into account the change in the gauge length. Therefore, as it has been expressed by Ling (Ling, 1996), we can obtain a relation between the true and the engineering strains under tension, through the expressions (4.12) and (4.14):

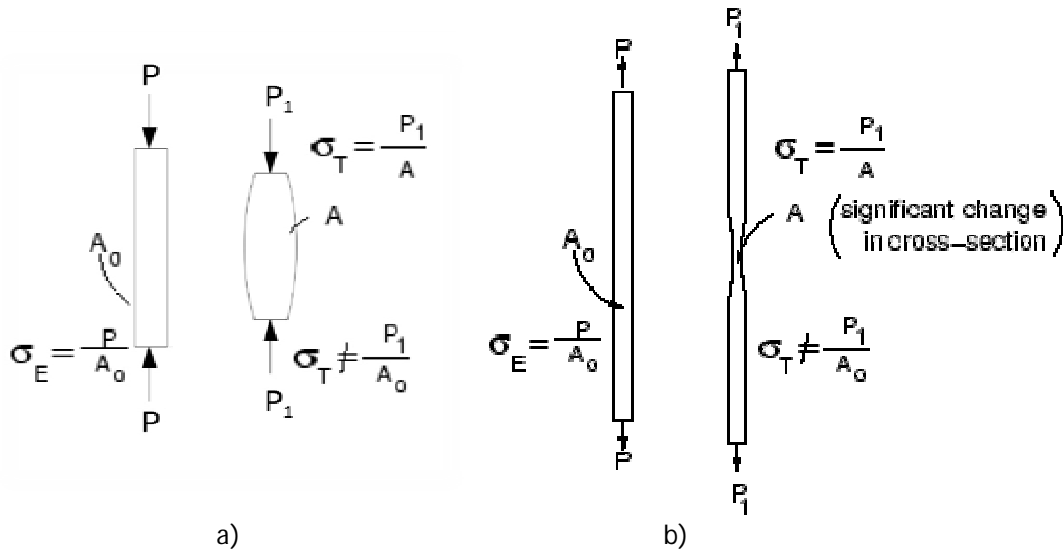
$$\varepsilon = \ln(1 + \varepsilon) \quad (4.15)$$

Then, knowing that the stress of a body can be obtained through the following expression (4.16):

$$\sigma_E = \frac{P}{A_0} \quad (4.16)$$

it can be quickly observed that for large strain ratios it becomes also necessary to update the value of stress, as the cross-sectional area of the tested specimen has changed notably. Then, if during a deformation the volume of the specimen remains constant, the true stress and the engineering stress can be related again through the following expression:

$$\sigma_T = \sigma_E(1 + \varepsilon) \quad (4.17)$$



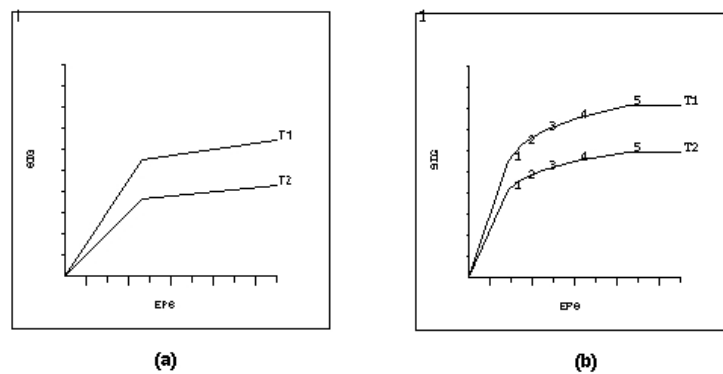
**Fig. IV.14 Growth and reduction of cross-sectional area in advanced strains.**

True stress varies from the engineering one in large strain ratios. [a] compression, [b] tension

Obviously, for the case of pure compression, the expressions (4.15) and (4.17) change the positive by a negative and then, the true stress is slightly lower than the apparent. This is caused by an increment of the transversal area of the sample in the middle height, contrary to the case of being subjected to tension. Owing to the need of analyzing specimens under large deformation axial loading [up to 25% strains in some cases], the true stress-strain curve for steel S355 in compression has been adopted. This curve is very similar to the apparent, but with a smoother decrease of stress respect to the first during the hardening period.

#### 4.4.1.2 Plasticity model used for steel.

A common constitutive model with two different variations, according to the needed accuracy, has been adopted in this investigation for steel: they are basically formed by a plastic hardening curve, combined with the von Mises yield Criterion. Depending on the requirements of each specific analysis, the *Bilinear Isotropic Hardening [BISO]* or the *Multilinear Isotropic Hardening [MISO]* has been used; the first one is based on a bilinear stress-strain curve, with no descending branch after yielding, and the second one is based on a multilinear stress-strain curve, defined by a significant yield plateau and an important hardening period. The first model is essentially an elastic perfectly-plastic model, whereby the collapse does never occur, while the latter is defined by an evolutionary stress-strain curve for the plastic hardening period.



**Fig. IV.15 Plastic hardening curves for the bilinear model [a] and the multilinear model [b]**

The use of the first model [much simpler than the latter] simplifies the mathematical convergence of the problem notably, since it is only based on two different linear functions. Then, in the elastic perfectly-plastic models which are presented in Chapter V, the first bilinear model has been used. For the rest, a multilinear curve has been considered instead. Needless to clarify that plasticity in both cases is always based on the von Mises yield criterion<sup>15</sup>.

To summarize, the code introduced in ANSYS to define the constitutive model used for steel [*MISO*, *Multilinear isotropic hardening*] takes the following form:

```
!Multilinear Isotropic Hardening Model for steel.
!General Parameters.
MPTEMP,,,,,,,,
MPTEMP,1,0
MPDATA,EX,2,,E
MPDATA,PRXY,2,,nu
TB,MISO,2,1,6,0
TBTEMP,0
TBPT,,0,0

!Plastic Hardening curve.
TBPT,,0.8*fy/210000,0.8*fy
TBPT,,fy/210000,fy
TBPT,,0.05,1.005*fy
TBPT,,0.1,1.006*fy
TBPT,,0.125,1.13*fy
TBPT,,0.15,1.27*fy
TBPT,,0.2,fy
TBPT,,0.25,0.9*fy
TBPT,,0.4,0.35*fy
```

where:

$f_y$	Yield limit stress
$E$	Elastic Young Modulus
$\nu$	Elastic Poisson's coefficient

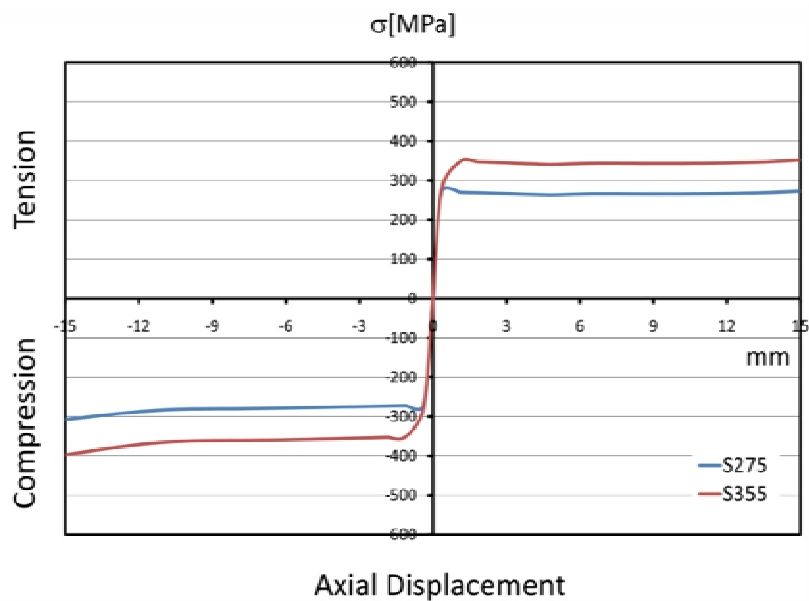
The same model defined in ABAQUS for S355 steel, is introduced through the following code:

<sup>15</sup> widely explained in Chapter II.

```
*STEEL S355
*Material, name=Steel
*Density
  7.85e-05,
*Elastic
210000., 0.29
*Plastic
284., 0.
355., 0.00169
356., 0.05
357., 0.1
402., 0.125
450., 0.15
350., 0.25
100., 0.4
```

#### Calibration of the constitutive model for steel.

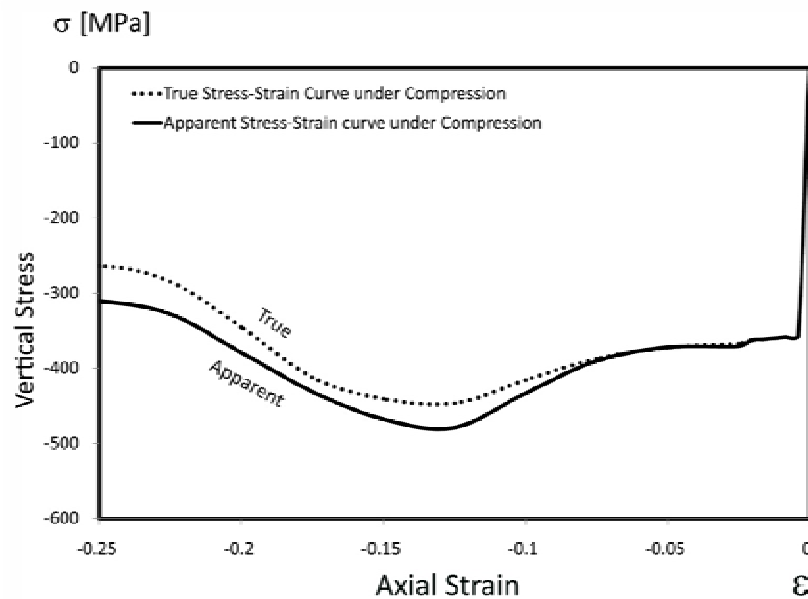
For verification purpose, a cylindrical specimen of 150 mm width and 300 mm height, according to Section 4.2.2, has been subjected to pure tension and compression tests. The results obtained can be observed in the following diagrams:



**Fig. IV.16 Stress-strain diagrams for steel of S355 and S275 strength.**  
Curves obtained using ABAQUS under tension [right] and compression [left].

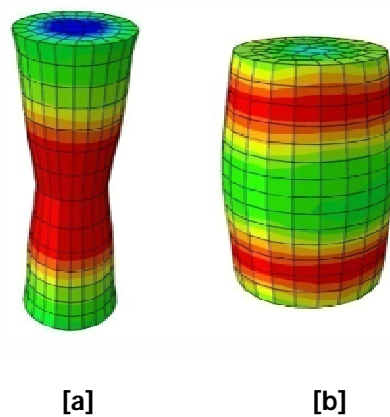
The behavior of steel can be considered almost symmetric under tension than under compression for low deformation ratios, as it can be seen from results obtained in the calibration process of figure IV.16. However, the large deformation axial response of steel is slightly different in each case, owing to the variation of the cross-sectional area. A large deformation axial test has been done, by using the same cylindrical specimen and assuming the apparent stress-strain curve first, and the true stress-strain curve later. The shape of the curves obtained is shown in figure IV.17:





**Fig. IV.17** Curves obtained using the *true stress* and the *apparent stress*-strain diagrams.  
Curves obtained from pure compression of a cylindrical simple of 150mm width.

The deformed shape before the collapse of the sample under tension is really different from the ultimate shape under compression, as it can be seen in figure IV.18. While in the first case the specimen suffers a drastic reduction of area in the middle-height, in the second case, the effects of the Poisson's ratio lead exactly to the opposite phenomenon. This is the reason why it is really important to take these increments or decrements into account, in order to reproduce the material behavior faithfully.



**Fig. IV.18** Deformed shapes under tension [a] and under compression [b].  
Tests of 300 mm height and 150 mm width specimens.

The deformed shapes of the tested specimens shown in Figure IV.18 a) and b) correspond to pure tension and compression tests. These tests have been done by embedding both edges and limiting all displacements and rotations to reproduce more reliably the real conditions of an experiment.

**4.4.2 Material models used for concrete.**

Due to the cohesive essence of concrete, this is a material which tends more to plasticity and nonlinearity than to a linear elastic behavior<sup>16</sup>. The plastic range in concrete is characterized for being extended and especially sensitive to the hydrostatic stress states -as in case of other cohesive materials. During the plastic hardening, concrete shows a progressive loss of stiffness which is converted into a capacity of energy absorption through the compressive damage -called *crushing*.

Besides, concrete is a material that clearly responds differently under tension than under compression. On the one hand, the description of the material response under tension requires the assumption of low strengths and complex cracking patterns; on the other hand, the definition of the evolutionary hardening law under compression may be quite complex since it is based on the combination of both yield and failure surfaces in the three-dimensional stress space.

As it has been mentioned before, this investigation has been following a gradual process to be capable of understanding the plastic behavior of concrete under high hydrostatic states. This is the reason why preliminary models were done using constitutive models based on perfect-plasticity [such as the Drucker-Prager yield criterion], and the rest were done using more complex damaged plasticity models. The fact of calibrating both material models to solve strictly the same problems and to compare the results with the experimental curves, is also one of the most interesting purposes of this investigation.

**4.4.2.1 General parameters adopted for concrete.**

The stress-strain curves and the maximum compressive strengths of concrete have been taken from those proposed in the American ACI<sup>17</sup> code, coming from multiple analytical and experimental studies carried out by different researchers such as (Popovics, 1973), (Martinez, et al., 1982) and (Ahmad, et al., 1985). These curves summarize all their contributions in reference to the initial elastic modulus and the softening descending branch of uniaxial compression tests.

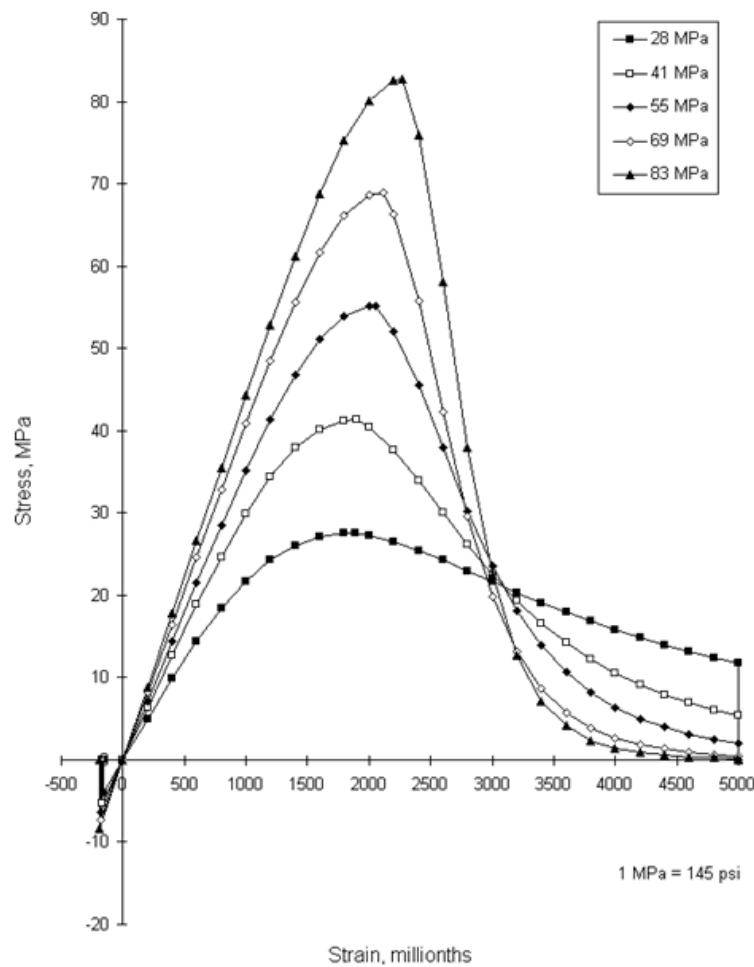
These curves have been chosen to define the constitutive models for concrete in this investigation, due to their precision and veracity [for all concrete strengths of 20, 30, 40 and 50 MPa], according to figure IV.19. It is well-known that those concretes with lower resistances [30 MPa] show an important ductility ratio, compared with those characterized by high strengths. As higher is the characteristic strength of a concrete, lower is its residual stress after softening.

As it will be explained in further Sections, the simplified stress-strain curves used in the material models for concrete to describe its uniaxial compressive response coincide with the curves proposed in the ACI American Code. These curves represent the complete stress-strain diagrams of different concretes, under tension and also compression. They are represented in the following figure IV.19 shown below:

---

<sup>16</sup> See Section 2.2.2

<sup>17</sup> State of the Art Report on High-Strength Concrete (ACI 363R-92)



**Fig. IV.19 Uniaxial stress-strain curves coming from experimental tests.**

Curves proposed by the *State of the Art Report on High-Strength Concrete* (ACI 363R-92)

Mechanical parameters considered for the elastic range of concrete are the initial elastic modulus [up to stresses of 50% of the  $f_{ck}$ ] and the elastic Poisson's ratio, according to Section 2.2.1 and (Husem, et al., 2007). Assuming that the elastic Poisson's ratio for stresses under 70% of  $f_{ck}$  is a constant value between 0.15 and 0.20 for any concrete strength, a value of 0.18 has been assumed for all cases. For the initial elastic modulus, the simplified expression (4.18) proposed in the ACI code (ACI, 1999) has been used:

$$E_c = 4700 \cdot \sqrt{f_{ck}} \quad (4.18)$$

#### 4.4.2.2 Previous considerations and preliminary models.

ANSYS provides a complex model to simulate the behavior of concrete which combines a yield surface<sup>18</sup> with a failure criterion, in order to limit the resistant capabilities under different loading conditions. This combination depends on nine different parameters which must be calibrated separately, especially in cases of high hydrostatic pressures. On the one hand, the yield surface

<sup>18</sup> It is based on the failure surface defined by William Warnke.

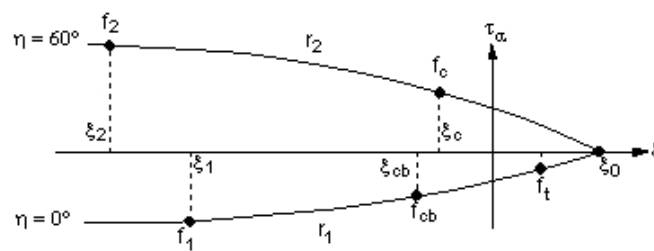
determines the plastic behavior of the material, while on the other hand the failure criteria limits the maximum stress at specific strain values for crushing under compression and cracking under tension.

As it has been mentioned, the “Concrete” constitutive model of ANSYS is defined by a collection of nine different parameters which must be calibrated separately, or adopted from other previous investigations instead. The calibration must be done for each stress state, and especially for those cases involving high hydrostatic pressures. The nine coefficients and their accepted values<sup>19</sup> are shown in Table IV.1:

**Table IV.1.** Variables needed to define the material model *concrete*.

Num.	Definition of the variable	Accepted value
1	Shear transfer coefficients for an open crack	0.5
2	Shear transfer coefficients for an closed crack	0.9
3	$f_t$ Ultimate uniaxial tensile strength	$0.09 * f_c$
4	$f_c$ Ultimate uniaxial compressive strength	$f_c$
5	$f_{cb}$ Ultimate biaxial compressive strength	$1.20 * f_c$
6	$\sigma_h$ Ambient hydrostatic pressure	Hydr. Stress State
7	$f_1$ Ultimate compressive strength for a state of biaxial compression superimposed on hydrostatic stress state	$1.45 * f_c$
8	$f_2$ Ultimate compressive strength for a state of uniaxial compression superimposed on hydrostatic stress state	$1.725 * f_c$
9	Stiffness multiplier for cracked tensile condition	0.6

Two cross-sectional planes of the failure surface used by the constitutive model “concrete” –based on the William Warnke criterion- are shown in figure IV.20, by matching five of the nine parameters defined before:



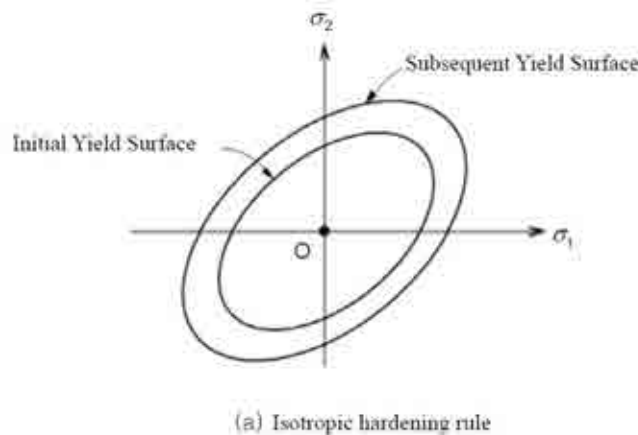
**Fig. IV.20** Cross-sections of the William-Warnke failure surface.

Graphical description of five of the parameters needed to define the constitutive model *Concrete*.

According to some literature about modeling concrete (Rangel Paes, 2003), first preliminary models have been analyzed by using different material models existing in ANSYS. Since the minimum possible failure surface can be defined through two parameters [ $f_t$ ,  $f_c$ ] only, the first and simplest material model used for concrete in this analysis is CONC+MISO. This model consists in a combination of the simplified failure criteria of the model “concrete” with a hardening stress-strain

<sup>19</sup> Ansys Theory Manual, (Kohnke, 2001).

curve defined by the *Multilinear Isotropic Hardening* [MISO]. It is curious to see how several studies focused on concrete have used this combination, although that MISO follows the von Mises yield criterion. Note that this constitutive model coincides with the one used for steel:



**Fig. IV.21 MISO model [Multilinear Isotropic Hardening]**  
The von Mises elliptical curve grows up concentrically.

For most numerical analyses involving concrete, in which the hydrostatic stress state is not really significant [such as the case of beam elements], the definition of concrete by using this combination may be enough reliable to reproduce its plastic behavior.

Thus, using the CONC+MISO combination for concrete, parameters 3 and 4 of Table IV.1 have been the only defined values in order to determine the maximum uniaxial tensile and compressive stresses. These parameters have been combined with a multilinear hardening stress-strain curve in order to describe the softening behavior beyond the peak of load. Since the von Mises cylindrical yield surface is not sensitive to the hydrostatic stress state, the volumetric expansion of concrete has not occurred in these preliminary models. Concrete subjected to high compressive loads tends to expand much more than lateral deformation predicted by its theoretical plastic Poisson's ratio. This expansion is governed by *dilatancy*, as a consequence of the internal microcracking<sup>20</sup>.

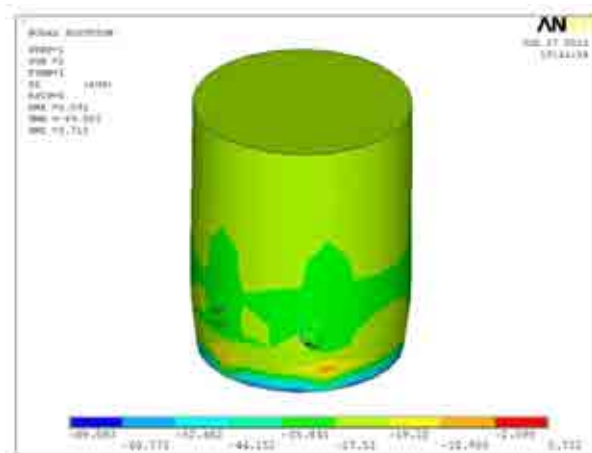
From results obtained, it can be concluded that the fact of using a model such as CONC+MISO for concrete is quite hazardous for those cases involving confinement. As lateral expansion of concrete is not faithfully reproduced due to the implementation of a cylindrical yield surface, the concrete of the core does not contact the tube, and confinement effect does not take place [see Section 4.2.1]. The code used to define this preliminary constitutive model for concrete in ANSYS [CONC+MISO] is the following:

```
!CONC+MISO model for concrete.
!General Elastic Parameters.
MPTEMP,,,,,,,,
MPTEMP,1,0
MPDATA,EX,1,,Ec
MPDATA,PRXY,1,,Nu
!
!Plastic hardening stress-strain curve for concrete [MISO]
TB,MISO,1,1,5,
```

<sup>20</sup> the *apparent* Poisson's ratio reaches values well above its maximum plastic value of 0.49, even up to 0.80-1.00, see Chapter II.

```
TBTEMP,0
TBPT,,0.0005,fc*0.5
TBPT,,0.001,fc*0.7
TBPT,,0.0015,fc*0.85
TBPT,,0.002,fc
TBPT,,0.003,fc*0.8
!
!Failure criteria [CONC]
TB,CONC,1,1,9,
TBTEMP,0
TBDATA,,.5,.9,ft,fck,,
TBDATA,,,,1,,,
MPTEMP,,,,,,,,
MPTEMP,1,0
```

In the following figure [Fig. IV.22], the deformed shape of concrete from one of these preliminary analyses is shown, by using the CONC+MISO model. Stresses reached by concrete coincide with its maximum compressive strength, and no confinement effect is detected. This is caused by the use of a cylindrical yield surface, which is clearly not pressure-sensitive; thus, when concrete and steel yields they follow their respective Poisson's ratio until a maximum value of 0.49, and the contact of both components does not occur.



**Fig. IV.22 Deformed shape of concrete core [concrete of 30MPa strength].**

Preliminary model using the MISO+CONC for concrete.

After having evaluated the CONC+MISO combination, the response of the material model *concrete* has been also analyzed alone, by using the William Warnke yield surface and calibrating all the nine variables mentioned in Table IV.1. Although these parameters are relatively well described in the literature for usual uniaxial states, no specific studies exist for cases involving high hydrostatic pressures. Actually, one of the parameters [number 6 in Table IV.1] curiously coincides with the hydrostatic stress state, a variable really difficult to be determined, especially when this state is variable (Rangel Paes, 2003).

#### 4.4.2.3 Elastic perfectly-plastic model with tension cutoff for concrete.

In order to guarantee the contact between the two components and, consequently, a suitable increment of strength provided by confinement effect, the combination CONC+MISO for concrete was discarded. Besides, the calibration of the nine variables of the constitutive model "*concrete*" results too complex for compressive states with high hydrostatic pressures. This is the reason why the next step in this investigation has been to change the MISO plasticity model -based on the von Mises cylindrical surface- by another one, based on the Drucker-Prager yield criterion -by using a conical surface. The fact of changing the cylindrical surface by a conical one is necessary in order to analyze cohesive materials, as this way yielding can be clearly pressure-sensitive to the hydrostatic state. Then, the next natural step has been to analyze the model with the combination of "*concrete*" with the Drucker-Prager yield criterion [CONC+DP]. This model is characterized for being elastic perfectly-plastic, neglecting the descending branch after yielding; this is just the reason why this combination does not require defining a hardening law in the plastic range.

##### General features of the model.

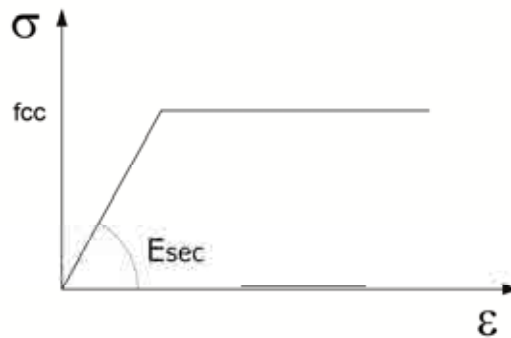
As it has been previously explained in Section 2.2.6.2, the Drucker-Prager yield criterion is one of the most suitable criteria to represent the plasticity behavior of concrete. Since it is based on a perfect conical surface, it is governed by its meridian which fully coincides with the Mohr-Coulomb linear function. The Mohr-Coulomb Criterion is defined by two variables: the internal friction angle ( $\varphi$ ) and the cohesion ( $c$ ), according to the following expression<sup>21</sup>:

$$\tau = c - tg\phi \cdot \sigma \quad (2.33)$$

This way, the plastic behavior of the material subjected to high hydrostatic pressures can be easily predicted assuming that  $\sigma_2 = \sigma_3$ ; in these cases, the compressive strength of concrete becomes considerably increased from  $f_c$  to  $f_{cc}$ , according to the postulates of Richart (Richart, et al., 1928):

$$f_{cc} = f_c + m \cdot \sigma_r \quad (2.19)$$

The CONC+DP model works elastic up to the value of the maximum confined stress,  $f_{cc}$ , from where it starts yielding perfectly-plastic, depending on lateral hydrostatic pressure. Since it refers to an elastic perfectly-plastic model, neither the descending branch nor the compressive failure of the material ever occurs.



**Fig. IV.23 Idealized stress-strain curve for concrete.**

Compressive response under hydrostatic pressure, according to perfect plasticity.

<sup>21</sup> see Section 2.2.6.1

This clearly elastic perfectly-plastic model is capable of reproducing the increment of compressive strength experimented by concrete faithfully, under confinement effect ( $f_{cc}$ ), although plasticity becomes infinite in this assumption, with no compressive crushing stress. This is the reason why it is impossible to determine a value of crushing stress under compression, and why concrete does not show softening after the peak of load. On the one hand, the limit of stress under tension can be easily superimposed to the Drucker-Prager yield criterion, by cutting the conical surface through a vertical plane coinciding with  $f_t$ ; the combination of the Drucker-Prager yield criterion with a minimum failure criterion defined by the parameter  $f_t$ , constitutes the mentioned elastic-plastic model with tension cut-off, known as CONC+DP.

As it can be observed in the code shown below, the maximum tensile stress of concrete has been limited to the 9% of the maximum compressive stress [expression (4.19)], coinciding with the third parameter of the nine necessary variables.

$$f_t \approx 0.09 * f_{ck} \quad (4.19)$$

$$f_c \approx -1 \quad (4.20)$$

The problem appears in case of pretending to generalize the methodology used for tension, also for compression. The fact of limiting the compressive maximum strength through parameters 4, 5, 7 and 8 becomes really impractical. The combination of the models CONC and DP in case of compression does not work really well, since it requires matching both yield and failure surfaces. This assumption becomes really complex if the aim is to succeed: the pretension of matching the value of  $f_{cc}$  [corresponding to the confined compressive strength] with the crushing strength defined by the failure surface is very difficult, since it requires making coincide two surfaces which are extremely close and sensitive (Rangel Paes, 2003). The solution to this problem lies in using a model limited in tension, but voluntarily perfectly-plastic in compression -unlimited plasticity. Since the minimum possible failure surface is formed by the two parameters, ( $f_c, f_t$ ), it is necessary to suppress the crushing capacity of the material by means of introducing the value -1 for the fourth parameter [expression (4.20)]. Then the code used for the CONC+DP model takes the following form:

```
!DP+CONC model for concrete
!General Parameters
MPTEMP,,,,,,,,
MPTEMP,1,0
MPDATA,EX,1,,Ecm
MPDATA,PRXY,1,,0.2
!*
!Failure criteria definition
TB,CONC,1,1,9,
TBTEMP,0
TBDATA,,,,0.09*fck,-1,,
TBDATA,,,,,,
!*
!Yield surface definition
TB,DP,1,,,
TBMODIF,1,1,c
TBMODIF,1,2,fi
TBMODIF,1,3,flow
```



where:

$c$	<i>Cohesion</i>
$f_i$	<i>Internal Friction Angle</i>
$f_{\text{flow}}$	<i>Flow Angle</i>

These three last variables become really important to calibrate the DP model, but the flow angle is especially decisive in case of modeling concrete-filled tubes, as this parameter governs the volumetric expansion of concrete. The flow angle determines the *dilatancy*, a parameter which is directly related to the volumetric expansion of the material in the plastic range. As it has been explained in Chapter II, the Poisson's ratio of concrete in the elastic period ranges from 0.15 to 0.20, while in plasticity this interval can grow up to 0.49. From experimental results, it is known that reality is quite different from theory: in the last stages of loading, concrete behaves not more exactly as a continuum material owing to the internal microcracking; its volumetric expansion becomes really more important than the deformation, predicted by its plastic Poisson's ratio. The *apparent* Poisson's ratio can reach values of 0.90, even 1.00 in some cases, according to Susantha and Ge (Susantha, et al., 2000) and Allos (Allos, et al., 1981).

#### Calibration of the determining variables.

The FE Models are extremely sensitive to the input parameters considered; results coming from a FE analysis can be easily erroneous depending on the exactitude of the input data. This is the reason why the three parameters mentioned before have to be calibrated separately by means of experimental results. The tests used for this calibration are those carried out by Schneider (Schneider, 1998) and Hu (Hu, et al., 2003) for sections made of 50 MPa concrete. For sections made of 30 MPa concrete, the experiments carried out by O'Shea and Bridge (O'Shea, et al., 2000) have been also used. All these mentioned specimens are short columns, being their geometrical and mechanical properties summarized in table IV.2:

**Table IV.2.** Material and geometrical features of the tests used.

Section	D*	t*	D/t	$f_c^{***}$	$f_t^{***}$	$N_{exp}^{**}$	Tested by
<b>CU-040</b>	200	5.00	40	27.15	265.80	2016.90	(Hu, et al., 2003)
<b>CU-047</b>	140	3.00	47	28.18	285.00	893.00	(Schneider, 1998)
<b>CU-070</b>	280	4.00	70	31.15	272.60	3025.20	(Hu, et al., 2003)
<b>S30CL50</b>	165	2.82	58.5	48.30	363.30	1759.00	(O'Shea, et al., 2000)
<b>S20CL80</b>	165	2.82	58.5	56.40	363.30	2040.00	(O'Shea, et al., 2000)

All values expressed in mm\*, kN\*\*, and N/mm<sup>2\*\*\*</sup>.

Being  $D$  the diameter,  $t$  the thickness and  $N_{exp}$  the experimental load.

To obtain the determining variables from the experimental tests mentioned before, the expression (2.81) provided by EC-4<sup>22</sup> has been used: for circular CFT short columns, the maximum load-bearing capacity of steel can be obtained through the following expression:

$$N_y = 0.75 \cdot A_y \cdot f_y \quad (4.21)$$

<sup>22</sup> Eurocode 4. (ENV1990-1-1, 1990)

As a consequence, the real strength of concrete core according to experimental tests, will be the following:

$$N_c = N_{exp} - N_y = A_c \cdot f_{cc} \quad (4.22)$$

By comparing the experimental response of concrete with its theoretical uniaxial compressive strength, we can observe that the first one is much higher than the latter:

$$N_{c,uni} = A_c \cdot f_c << A_c \cdot f_{cc} \quad (4.23)$$

Therefore, the proportion between the maximum compressive strength of confined concrete and the characteristic strength corresponding to unconfined concrete, can be easily calculated through:

$$\frac{f_{cc}}{f_c} = \frac{N_{exp} - N_y}{N_{c,uni}} \quad (4.24)$$

Analyzing this value by using the mentioned expression proposed by Richart (Richart, et al., 1928):

$$f_{cc} = f_c + m \cdot \sigma_r \quad (2.19)$$

and at the same time knowing the approximate value of lateral pressure  $\sigma_r$ , provided by the tube on the core, through the well-known expression proposed by Susantha, together with Ge (Susantha, et al., 2000):

$$\sigma_r = f_r = \beta \cdot \frac{2 \cdot t}{D - 2 \cdot t} \cdot f_y \quad (4.25)$$

Where  $\beta$  is the difference between the Poisson's ratios of the composite section and the concrete core, respectively:  $\beta = \nu_e - \nu_s$ , being  $\nu_s = 0.5$  [maximum plastic Poisson's ratio for steel] and  $\nu_e$  the maximum *apparent* Poisson's ratio of the composite section. Lateral pressure  $\sigma_r$  can be easily measured in circular CFT sections, owing to its uniformity provided by tube<sup>23</sup>.

Then, according to Susantha and Ge again (Susantha, et al., 2000), the maximum apparent Poisson's ratio of the composite section can be calculated by using the following expressions, derived from experimental tests:

$$\nu_e = 0.2312 + 0.3582 \cdot \nu'_e - 0.1524 \cdot \left[ \frac{f_c}{f_y} \right] + 4.843 \cdot \nu'_e \cdot \left[ \frac{f_c}{f_y} \right] - 9.169 \cdot \left[ \frac{f_c}{f_y} \right]^2 \quad (4.26)$$

$$\nu'_e = 0.881 \cdot 10^{-6} \cdot (D/t)^3 - 2.58 \cdot 10^{-4} \cdot (D/t)^2 + 1.953 \cdot 10^{-2} \cdot (D/t) + 0.4011 \quad (4.27)$$

Thus, for specimens of Table IV.2, the values of lateral pressure,  $\sigma_r$ , the apparent Poisson's ratio of the composite section,  $\nu_e$ , the value of coefficient,  $\beta$  and the value of coefficient  $m$  of expression (2.19) are the following:

<sup>23</sup> see Section 2.3.1

**Table IV.3.** Material and geometrical features of the tests used.

Section	$f_c^*$	$f_y^*$	$N_{exp}^{**}$	$N_y^{**}$	$N_{c,exp}^{**}$	$N_c^{**}$
CU-040	27.15	265.80	2016.90	610.62	1406.28	769.78
CU-047	28.18	285.00	893.00	275.99	617.01	397.41
CU-070	31.50	272.60	3025.20	709.10	2316.10	1810.03
Average	28.82	274.47				
S30CL50	48.30	363.30	1759.00	391.49	1367.51	963.38
S20CL80	56.40	363.30	2040.00	391.49	1648.51	1124.94
Average	52.40	363.30				

All the values are in N/mm<sup>2</sup>\* and kN\*\*

**Table IV.4.** Material and geometrical features of the tests used.

Section	$f_{cc}/f_c$	ve'	ve	$\beta$	$\sigma_r^*$	$m$
CU-040	1.83	0.83	0.82	0.32	4.54	4.95
CU-047	1.55	0.84	0.83	0.33	4.21	3.70
CU-070	1.28	0.81	0.83	0.33	2.64	3.30
Average		0.82	0.83			3.98
S30CL50	1.42	0.84	0.89	0.39	4.98	4.07
S20CL80	1.47	0.84	0.92	0.42	5.34	4.91
Average		0.84	0.90			4.49

The values are in N/mm<sup>2</sup>\*.

From results obtained and shown in Tables IV.3 and IV.4, we can consider a value of 4.2 for coefficient  $m$  [the average between the obtained values for 30MPa and 50MPa concrete], which coincides with the values provided by several authors of literature, such as Richart (Richart, et al., 1928) and Chen (Chen, 1982).

Assuming a value of 4.2 for coefficient  $m$  in the Richart expression, and knowing the maximum compressive uniaxial strength of concrete, three different Mohr circles have been obtained [named 1, 2 and 3] for 30 MPa concrete, and three more circles [4,5 and 6] for 50 MPa concrete, by assuming three different hydrostatic states [of 0, 3 and 5 MPa]. Then, by using the expressions shown in Sections 2.2.6.1 and 2.2.6.2 of this text, the parameters for internal friction angle and cohesion can be easily calculated in both cases:

$$m = \frac{f'_c}{f'_t} \rightarrow f'_t = \frac{28.82}{4.2} = 6.85 \text{ MPa} \quad (4.28)$$

$$m = \frac{f'_c}{f'_t} \rightarrow f'_t = \frac{52.40}{4.2} = 12.47 \text{ MPa} \quad (4.29)$$

using also the expressions (2.39) and (2.40):

$$f'_c - f'_c \cdot \sin\phi = 2 \cdot c \cdot \cos\phi \quad (4.30)$$

$$f'_t + f'_t \cdot \sin\phi = 2 \cdot c \cdot \cos\phi \quad (4.31)$$

and finally equating both expressions, it is possible to calculate the value of  $\phi$ :

$$\phi = \arcsin\left(\frac{f'_c - f'_t}{f'_c + f'_t}\right) \quad (4.32)$$

In the same way, also the value of cohesion can be obtained from expressions (4.30) and (4.31):

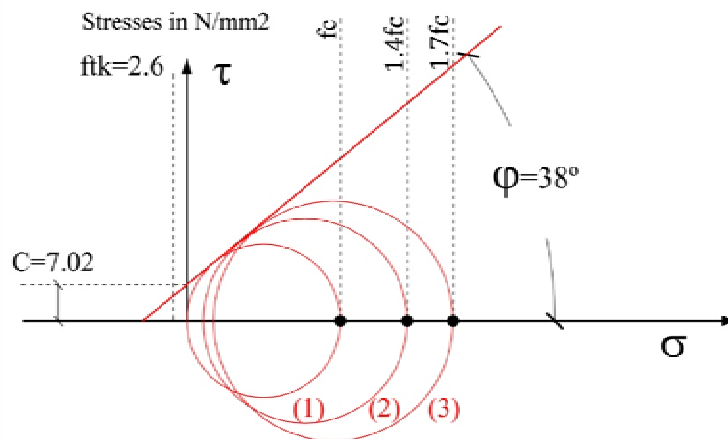
$$c = \frac{f'_c - f'_c \cdot \sin\phi}{2 \cdot \cos\phi} \quad (4.33)$$

Thus, we obtain for both concrete strengths a set of determining parameters which also coincide with those proposed by literature, (Lu, et al., 2006) and (Fujita, et al., 1998):

**Table IV.5.** Material and geometrical features.

Section	c	$\phi$
30 MPa	7.023	38
50 MPa	12.78	38

\* Cohesion expressed in  $\text{N/mm}^2$  and  $\phi$  in degrees.



**Fig. IV.24** Circles of Mohr 1,2 and 3 calculated for concrete of 30MPa.

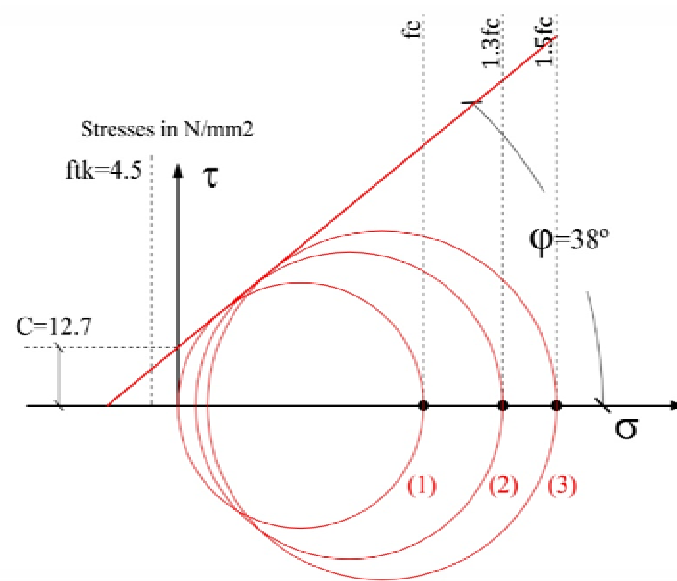


Fig. IV.25 Circles of Mohr 4,5 and 6, calculated for concrete of 50MPa.

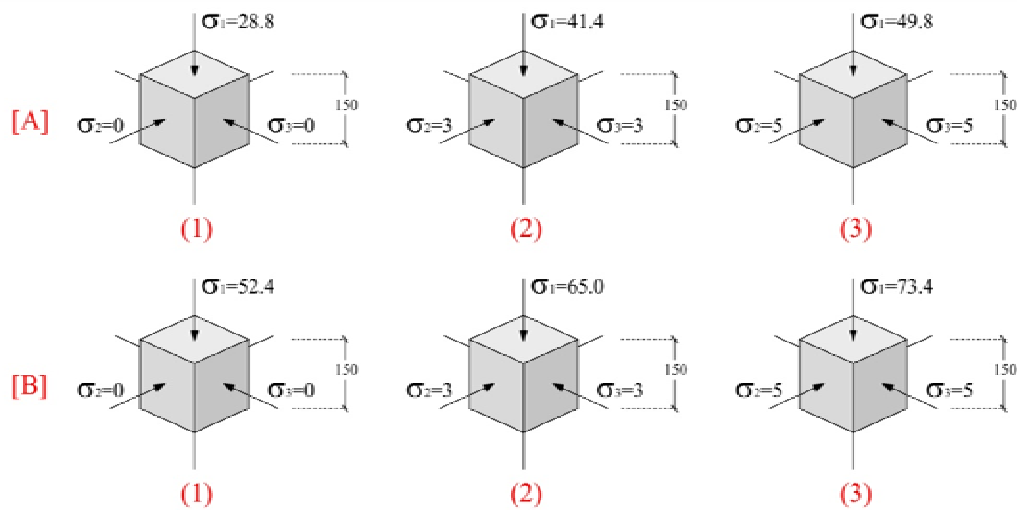
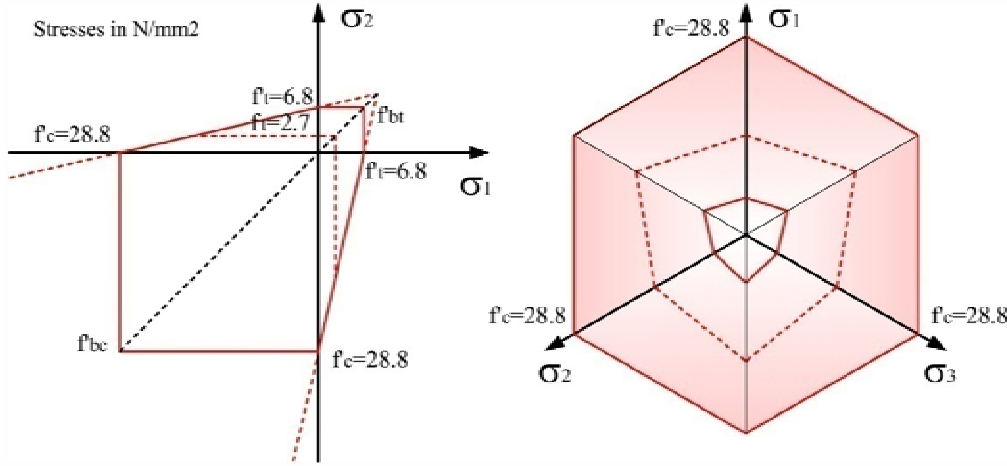


Fig. IV.26 Hydrostatic states considered for each circle of Mohr.

$\sigma_1$  corresponds to the confined strength of concrete  $f_{cc}$ .

From the values obtained in the experimental tests, and using the expressions provided in Section 2.2.6.1, it is possible to represent the hexagonal surface of the Mohr-Coulomb yield criterion in the three-dimensional stress space. This surface can be drawn by using the key points which define the characteristic uniaxial tensile and compressive strength of concrete, as well as under biaxial states.



**Fig. IV.27 Three-dimensional matching of the Mohr-Coulomb hexagonal surface.**

Values obtained from experimental tests of CFT sections presented in Table V.2.

To convert the Mohr-Coulomb hexagonal surface [represented in fig. IV.27] into the Drucker-Prager conical surface on the  $\theta = 60^\circ$  angle, two constants derived from the internal friction angle and cohesion are needed [ $\alpha$  and  $k$ ]. The expressions used to calculate their value vary depending on the considered points of the Mohr-Coulomb surface; in case of the cone on the  $\theta = 60^\circ$  plane, matching points are  $f'_{bt}$  and  $f'_c$ :

$$\alpha = \frac{2 \cdot \sin \phi}{\sqrt{3} \cdot (3 - \sin \phi)} \quad (4.34)$$

$$k = \frac{6 \cdot c \cdot \cos \phi}{\sqrt{3} \cdot (3 - \sin \phi)} \quad (4.35)$$

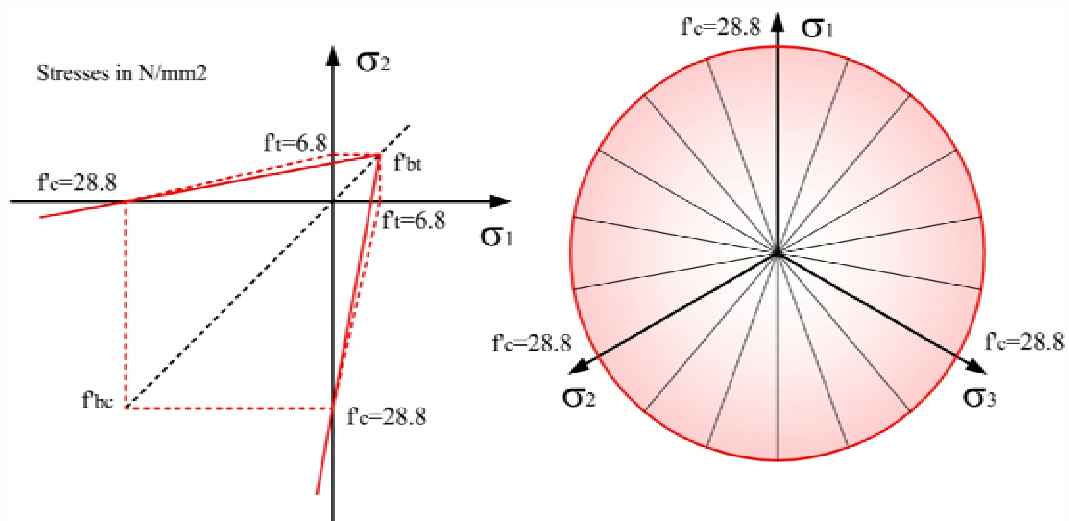
Then, for 30MPa concrete:

$$\alpha = 0.298 \quad \text{and} \quad k = 8.04 \quad (4.36)$$

and for 50MPa concrete:

$$\alpha = 0.298 \quad \text{and} \quad k = 14.63 \quad (4.37)$$

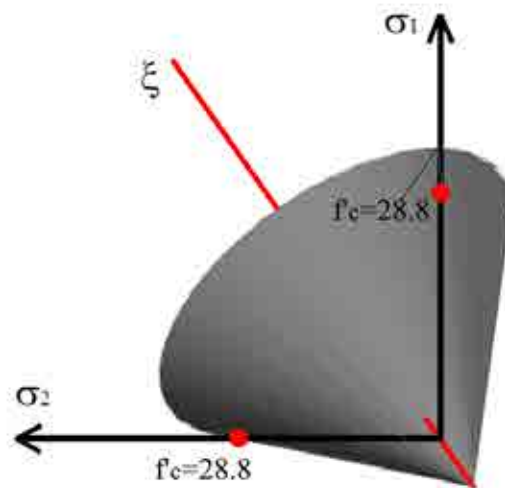
To replace the hexagonal surface of figure IV.27 by a conical surface, the obtained values (4.36) and (4.37) coming from the available experiments have been used, The final conical surface in the biaxial plane, according to the Drucker-Prager yield criteria, has the following form of Fig. IV.28:



**Fig. IV.28 Three-dimensional matching of the Drucker-Prager conical surface.**

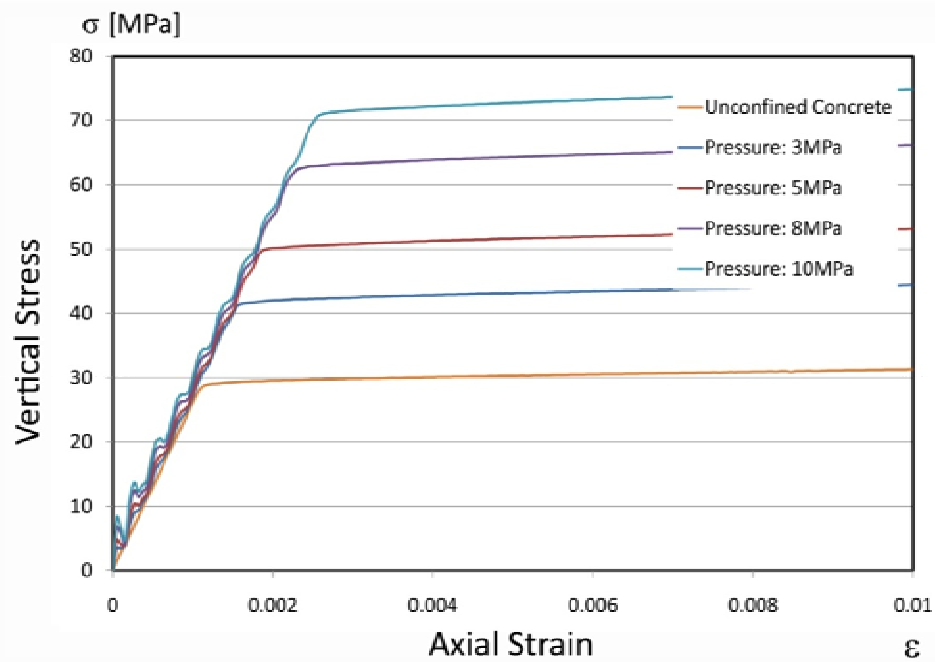
Generalization of the hexagonal Mohr-Coulomb surface shown in figure IV.27.

Its representation in the three-dimensional stress space:



**Fig. IV.29 Tridimensional representation of the obtained Drucker-Prager conical surface.**

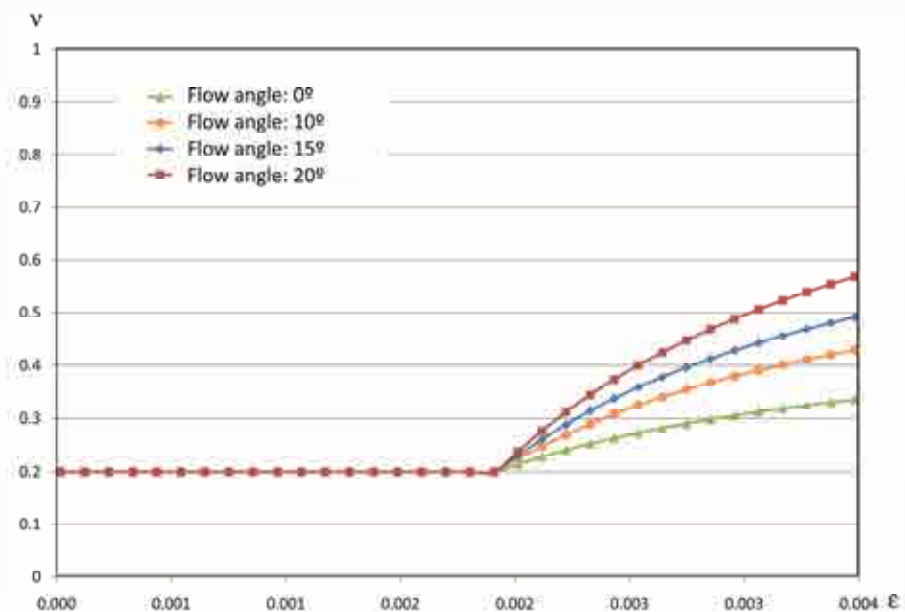
Although these values work really well for the previously mentioned cases, it is important to point out that the defined yield surface is very sensitive to the input parameters. To finalize the process, a numerical verification has been carried out by using a cubic specimen of 150 mm width. The test has been repeated under five different hydrostatic compressive states [where  $\sigma_2 = \sigma_3$ ].



**Fig. IV.30 Calibration of the Drucker-Prager constitutive model by ANSYS**

It is shown how results are sensitive to the hydrostatic ambient state.

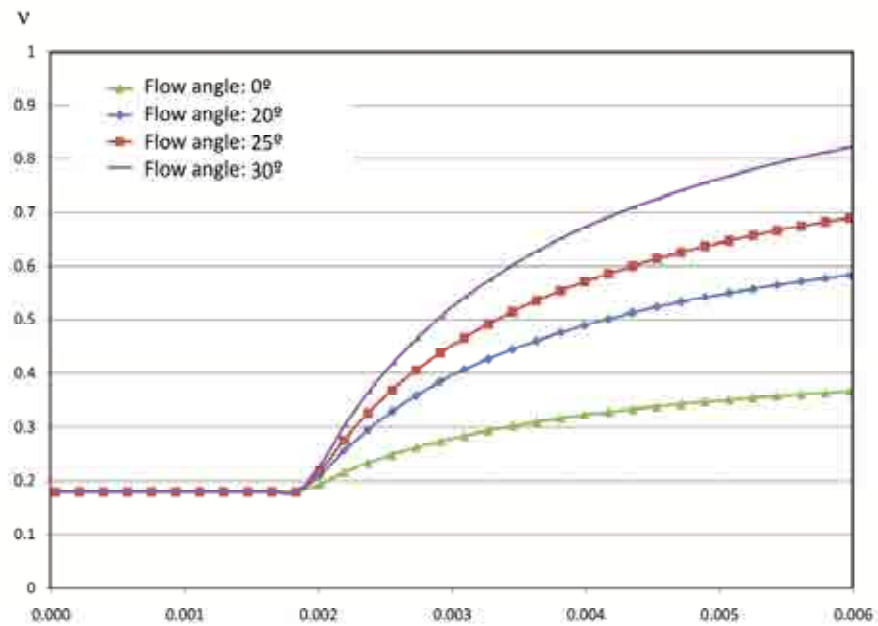
To calibrate the third variable [the flow angle], the expression (4.27) for lateral deformation ratio and proposed by Susantha (Susantha, et al., 2000) has been used. The values of the *apparent Poisson's ratio* obtained in Table IV.4 range from 0.81 to 0.84: it is obvious that these values are well above the maximum plastic Poisson's coefficient, derived from theory [0.49]. We know that the flow angle is decisive to determine the volumetric expansion of concrete in plasticity; a cubic specimen of 150 mm width has been analyzed under different hydrostatic pressures, in order to obtain the ratio of lateral deformation respect to vertical strain.



**Fig. IV.31 Diagrams  $\nu_{app} - \epsilon$  for 50MPa concrete.**

Curves of the apparent Poisson's ratio depending on vertical strain, in a uniaxial stress state.





**Fig. IV.32 Diagrams  $v_{app} - \epsilon$  for 50MPa concrete.**

Curves of the apparent Poisson's ratio depending on vertical strain, under pressure of 5 MPa.

By assuming that the *apparent Poisson's ratio* under a hydrostatic pressure of 5MPa ranges from 0.81 to 0.84 [as it is derived from experimental tests in Table IV.4], the unique curve of figure IV.32 which tends to these values in advanced plasticity is that corresponding to a flow angle of 30°. According to literature, for a non-associative flow rule, the dilatancy angle is always lower than the internal-friction angle of the material, (Mirmiran, et al., 2000); thus, a flow angle of 30° coincides accurately with theory and experimental tests. This is the reason why a value of 30° has been considered for the flow angle in the models done with the Drucker-Praguer yield criterion.

#### 4.4.2.4 Damaged Plasticity Model for Concrete [DPC]

A second constitutive model has been used for concrete with the final objective of achieving the most realistic reproduction of the cohesive material as possible, especially to incorporate also crushing and softening behaviors to the yield criteria. The principal difference between this model and the elastic perfectly-plastic models, based on the Drucker-Praguer criterion, is the precision of the first one in the definition of concrete behavior beyond the peak of load. The fact of introducing an evolutionary damage criterion in the model does not provide any extra information about the load-bearing capacity of concrete, but it is crucial to determine the post-peak behavior<sup>24</sup>.

This second model has been implemented by using the commercial software ABAQUS Explicit, through the constitutive material model known as "*Plasticity Damage for Concrete*". This model available in ABAQUS is tridimensional, and it is based on the damage plasticity model proposed 20 years ago by Lubliner and Oller (Lubliner, et al., 1989), and modified later by Lee and Fenves (Lee, et al., 1998). It is capable of simulating the material behavior under high compressive hydrostatic states, and also under tension. To define this model it is necessary to determine the determining parameters of the yield surface and the two stress-strain curves of plastic hardening, under the assumptions of pure tension and pure compression; besides, two evolutionary damage laws have to

<sup>24</sup> see Section 2.2.7

be also defined under both states. This way, the behavior of concrete can be widely determined: in the first range [up to 50%  $f_{ck}$ ], the material behaves elastic, from where yielding occurs involving a damage process, due to the progressive appearance of crushing. The descending branch under compression tends to be parabolic, while this descent under tension is clearly exponential<sup>25</sup>.

**Definition of the determining parameters of the yield surface.**

The yield surface can be easily governed through two known variables:  $K_c$  and  $\sigma_{bo}/\sigma_{c0}$ . The first one describes the shape of the deviatoric plane [Fig. II.9], while the latter describes the proportion between the maximum biaxial compressive strength and the maximum uniaxial strength. The model uses a non associative flow rule<sup>26</sup> to describe the plastic strain increments, and flow potential is governed by the Drucker-Prager hyperbolic function. To finalize the definition of the complete material behavior, three more variables are needed: the dilation angle, the eccentricity and the viscosity parameter. No doubt that the decisive variable of these last three values is the dilation angle, since it determines the dilatancy in plasticity, being crucial in those cases in which confinement effect is involved. In this study, a dilation angle of 31° has been used, coming from the analysis of the previous paragraph and several experimental studies of existing literature, such as those of Starossek (Starossek, et al., 2008) and (Kuang, et al., 2010). The assumed value for the dilation angle can vary considerably depending on the purpose of the analysis: in case of concrete subjected to high hydrostatic states, this parameter must be considered according to its maximum value, which is about 31° (Prato, et al., 2003). This value coincides accurately with the results obtained in the previous paragraph.

The two other parameters come directly from literature, (Starossek, et al., 2008). They have been validated experimentally by other researchers: the aim is to achieve the most accurate model for concrete in order to solve the proposed problems, with the minimum processing effort and the maximum mathematical convergence. A value of 0.1 has been taken for eccentricity and even lower values for viscosity, in order to maximize the mentioned convergence. Thus, the final code introduced to define the yield surface of concrete in the DPC model is:

```
*Concrete Damaged Plasticity
31., 0.1, 1.16, 0.65, 0.01
```

**Definition of the plastic hardening curves.**

The behavior of concrete under tension is completely opposite to its behavior under compression, in terms of strength and damage evolutionary process. Under uniaxial compression, the material reaches its maximum strength by following a parabolic function, decreasing afterwards smoothly through the absorption of an important amount of energy of fracture; otherwise, under tension, the growth is completely linear and the descent follows an exponential function, instead. These two behaviors have been accurately described through experimental tests by Jankowiak and Lodigovsky (Jankowiak, et al., 2005) among others, and reformulated by Castro (Castro Medina, 2011)<sup>27</sup>, using the energetic method.

The DPC constitutive model available in ABAQUS allows defining both behaviors separately, by specifying a different plastic hardening descent under compression than under tension. Although the behavior of concrete under both uniaxial states is clearly determined by these hardening laws, the post-peak behavior is not so simple. It is known that concrete collapses sharply under tension,

---

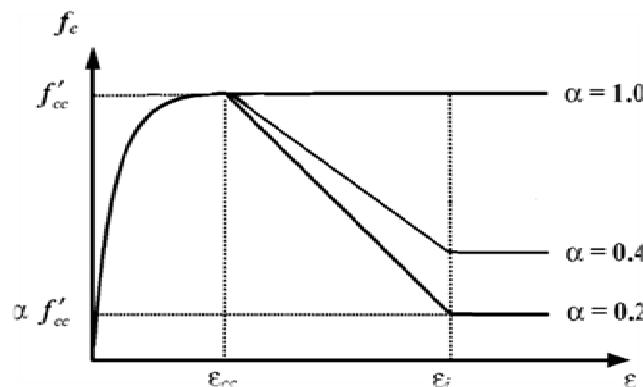
<sup>25</sup> see Section 2.1.7.1

<sup>26</sup> see Section 2.2.5.2

<sup>27</sup> see Section 2.1.7.1

by following an exponential function; however, this collapse does not occur exactly in this way under compression, where concrete can have different descending branches depending on the hydrostatic stress state<sup>28</sup>. From curves presented in figure IV.19, it can be derived that high strength concretes [corresponding to strengths over 40 MPa] tend to show a sharper descent of stress, and a lower residual stress ( $\alpha$ ) about 10%-15% of its maximum compressive strength; however, this assumption is true for uniaxial tests only, but not for those cases of concrete subjected to confinement.

The Japanese researcher Susantha (Susanta, et al., 2000) proposed a set of simplified expressions to determine the angle of descending branch Z, and the value of the residual stress,  $\alpha$ , under different hydrostatic states, derived from several experimental tests done by other researchers. Thus, this analytical model has been compared to the stress-strain curves obtained in this investigation with a surprising agreement of results.



**Fig. IV.33 Idealization of the plastic hardening descent of confined concrete.**  
(Susanta, et al., 2000)

Then, the codes introduced in ABAQUS to define the compressive and the tensile hardening laws take the following form:

For concrete of 30 MPa strength:

```
*Concrete Compression Hardening
15., 0
18., 0.0003
22., 0.0005
25., 0.0007
30., 0.0013
27., 0.0023
15., 0.0043
```

```
*Concrete Tension Stiffening
2.7., 0.
0.1, 0.002
0.01, 0.003
```

For concrete of 40 MPa strength:

```
*Concrete Compression Hardening
```

<sup>28</sup> see Section 2.2.7

```

20., 0.
25., 0.0004
30., 0.0006
35., 0.0008
40., 0.0010
40., 0.0014
16., 0.0250

```

\*Concrete Tension Stiffening

```

3.6., 0.
0.1, 0.002
0.01, 0.003

```

For concrete of 50 MPa strength:

\*Concrete Compression Hardening

```

20., 0.
25., 0.0003
30., 0.0005
35., 0.0007
40., 0.0009
45., 0.0011
50., 0.0015
1., 0.0250

```

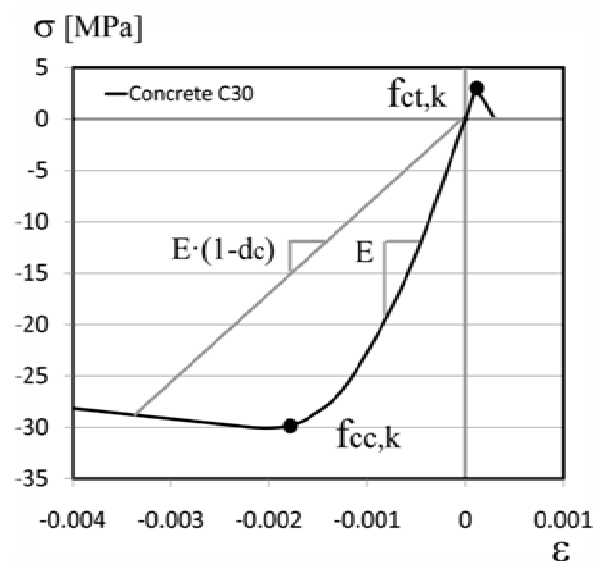
\*Concrete Tension Stiffening

```

4., 0.
0.1, 0.002
0.01, 0.003

```

Obviously, the behavior of concrete in the first stage of loading up to the first point of the hardening law under compression [corresponding to the 50% of the compressive strength] is governed by the elastic Young modulus and the elastic Poisson's ratio. From this point, concrete starts a damage process which will be more accurately described in the following Section.



**Fig. IV.34 Complete plastic hardening law considered [compression and tension].**  
Obviously, the plastic softening and the residual stress will depend on the steel recipient.

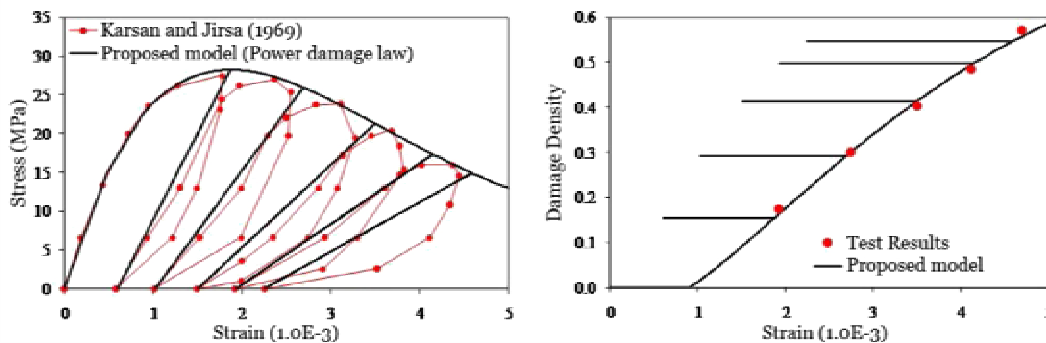
### Definition of the evolutionary damage ratio laws.

Laws for the plastic hardening behavior under tension and compression are not enough to reproduce the complexity of the structural response of concrete. From a value of stress of the 50% of the maximum compressive uniaxial strength, concrete starts a damage process which is characterized for its irreversibility. From an advanced point of loading process, concrete initiates a crushing process due to microcracking of the cement paste, characterized by absorbing a high percentage of energy; the percentage of damaged material is not capable of being reloaded.

With the objective of completing the definition of the input data for the *Concrete Damaged Plasticity* model [DPC], it is necessary to introduce also two evolutionary damage laws under tension and under compression [according to figure II.12, see Section 2.2.7]. The energy of fracture is really much more important under compression [especially in confined concrete] than under tension. The percentage of damaged concrete is represented by the scalar factor,  $d_c$ , ranging from 0 to 1. As in case of the stress-strain hardening laws in plasticity, those curves which define the evolutionary damage ratio are also different for tension than for compression. As it is explained in Chapter II, parameter  $d_c$  affects the plastic stress and the material stiffness in the following form [see Section 2.2.7.1]:

$$E_p = (1 - d_c) \cdot E_0 \quad (4.38)$$

The evolution of the damage evolutionary ratio has been investigated by several authors, such as Karsan and Girsan (Karsan, et al., 1969), Sadrnjad (Sadrnjad, 2012), (Liu, et al., 2009) and (Ludovic, et al., 2004), all them with different purposes. In this analysis, the values proposed by the first author have been used for concrete of 30MPa, and they have been extrapolated to other concrete strengths by using the correlations obtained by Susantha (Susantha, et al., 2000). The evolutionary damage ratio is also pressure-sensitive, as in case of the evolutionary stress laws:



**Fig. IV.35 Damage evolutionary analysis of concrete, coming from experimental tests.**  
(Karsan, et al., 1969)

Then, the code introduced in ABAQUS in order to define the curves corresponding to the evolutionary damage ratio for each different concrete:

For concrete of 30 MPa:

```
*Concrete Compression Damage
0., 0.
0.25, 0.0012
0.60, 0.0250
```

```
*Concrete Tension Damage, compression recovery=0.95
0., 0.
0.25, 0.0005
0.60, 0.0020
0.95, 0.0030
```

For concrete of 40 MPa:

```
*Concrete Compression Damage
0., 0.
0.20, 0.0014
0.60, 0.0250
*Concrete Tension Damage, compression recovery=0.95
0., 0.
0.25, 0.0005
0.60, 0.0020
0.95, 0.0030
```

For concrete of 50 MPa:

```
*Concrete Compression Damage
0., 0.
0.20, 0.0015
0.60, 0.0250
*Concrete Tension Damage, compression recovery=0.95
0., 0.
0.25, 0.0005
0.60, 0.0020
0.95, 0.0030
```

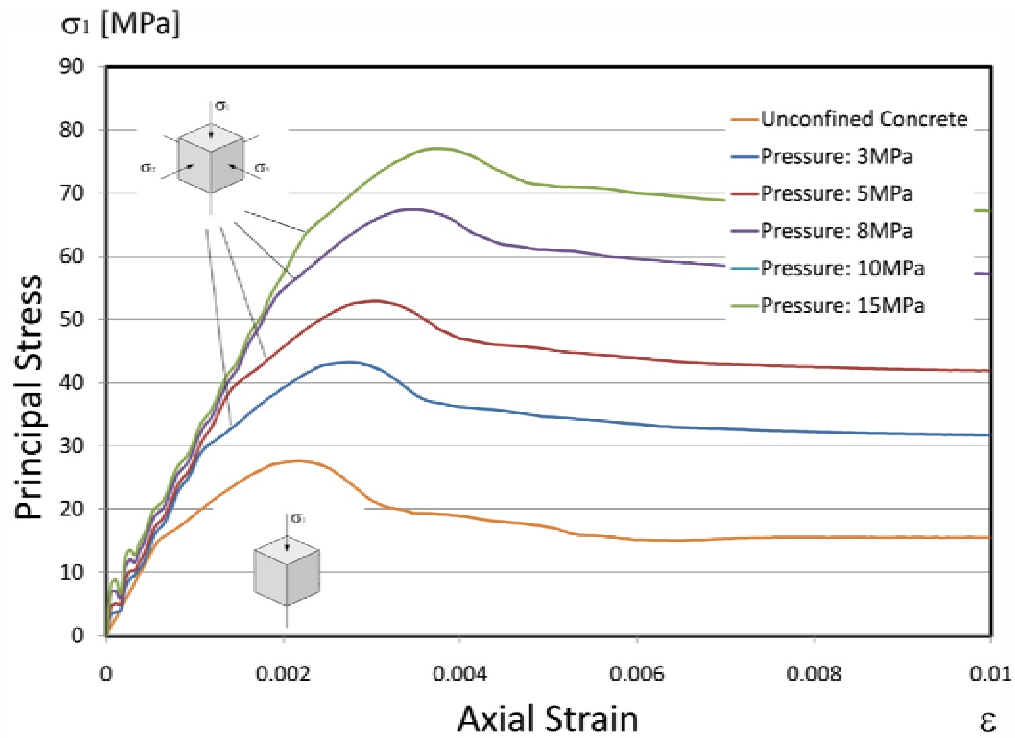
It is important to highlight that to have a point of view about the evolution of damage is more accurate than having an isolated tensional conception alone. Once concrete is crushed, the material becomes irreversibly damaged although it can keep vertical load completely constant, or even increase it due to confinement effect. This phenomenon will be widely explained and shown in the next two Chapters.

#### **Calibration of the DPC<sup>29</sup> model.**

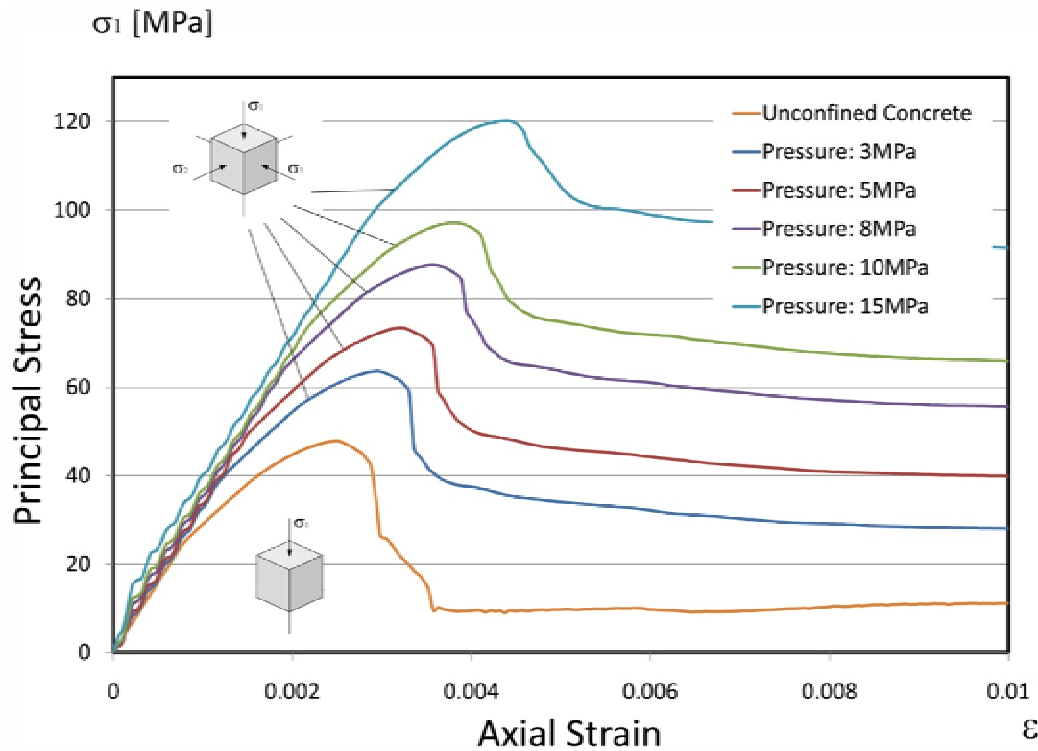
Finally, this complex constitutive model has been calibrated using two cubic specimens of 150 mm width with 30 and 50MPa strengths, like for the case of elastic perfectly-plastic constitutive models. To verify that this model is really sensitive to hydrostatic stress states, the mentioned specimen has been subjected to different triaxial compressive states of 3, 5, 8, 10 and 15 MPa pressures. The obtained results have been compared with those coming from the unconfined uniaxial stress-strain curve.

---

<sup>29</sup> *Damaged Plasticity Model for Concrete.*



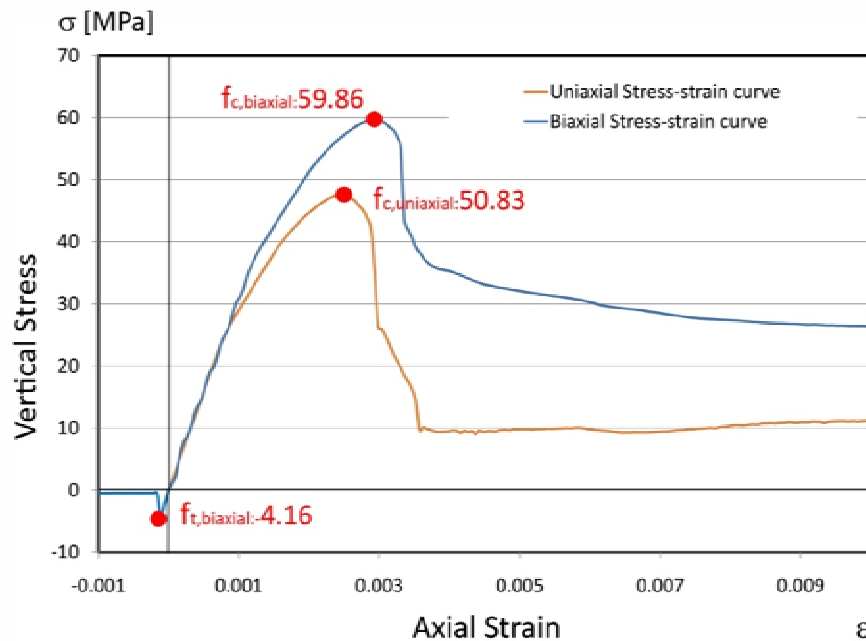
**Fig. IV.36 Calibration of the Damaged Plasticity model for concrete in ABAQUS.**  
Different stress-strain curves under different hydrostatic states, for 30MPa concrete.



**IV.37 Calibration of the Damaged Plasticity model for concrete in ABAQUS**  
Different stress-strain curves under different hydrostatic states, for 50MPa concrete.

Besides, singular points of the complete failure surface of concrete have been checked using the DPC model, described before. Two complete stress-strain curves for uniaxial and biaxial states of 50MPa concrete have been obtained from pure compression and tension tests. It is evident that the angle of the descending branch [as well as residual stress] depends directly on confinement; this assumption can be observed in figures IV.36 and IV.37, where the analyses corresponding to higher hydrostatic pressures show smoother descents after the peak of load.

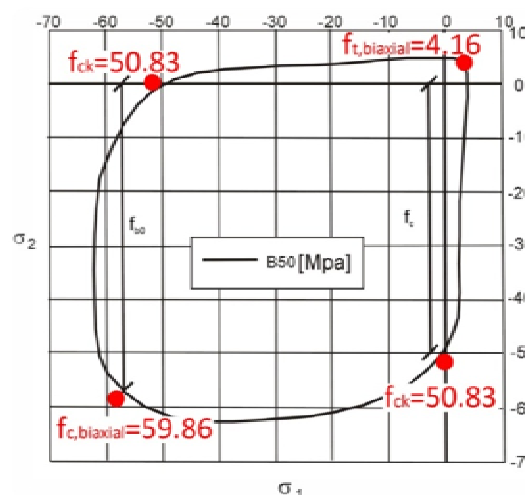
The case of concrete subjected to a compressive biaxial stress state has been also calibrated separately. Note that the increment of compressive strength is about 16% more, and that softening of concrete is drastically reduced by means of biaxial pressure [see figure IV.38].



**IV.38 Uniaxial and Biaxial complete stress-strain curves.**

The analysis has been done for a 50 MPa concrete.

The characteristic values of stress, obtained from the FE analysis, have been superimposed on the biaxial plane; full coincidence is observed with the experimental curve:



**IV.39 Full coincidence is observed between the obtained results and the experimental failure surface in the biaxial plane.**



#### 4.4.3 Contact model to reproduce the interaction between components.

To reproduce the contact interaction between the two components in case of concrete-filled tubes, two different criteria have been established: one for the normal component and other for the tangential component.

##### 4.4.3.1 Normal contact.

The model used to represent the normal component of contact is really simple and it is known in ABAQUS software as *"Hard Contact"*: the algorithm identifies whether the two components are in contact or not without any implemented criteria for physical or chemical adherence. The truth is that this adherence between components really exists, but it is not definitively significant over the compressive response of the composite section. This is the reason why most authors of the existing literature do not take this adherence into account.

In the analysis, no gap has been considered between the steel tube and the core initially. The two materials have been loaded simultaneously, being in contact from the first moment, and the hypothetic detachment of components is due to the difference in transversal strain experimented by each different material, in any case.

##### 4.4.3.2 Tangential contact.

Otherwise, tangential contact must be considered separately, by assuming a specific friction coefficient. Sliding of one material respect to the other may be significant, especially when local buckling occurs. Tangential component of contact has been defined by using the available model *"Penalty"*, of ABAQUS and ANSYS libraries. The use of a specific model for tangential contact leads to consider the friction forces generated in the interface, governing the sliding of one component respect to the other. The magnitude of tangential stresses appeared on the interface can be obtained by using the following expression:

$$\tau = \mu_{st} \cdot \sigma_{normal} \quad (4.39)$$

where  $\mu_{st}$  is the static friction coefficient, defined as 0.2 between steel and concrete, according to Eurocodes and the existing literature.

The value of the friction coefficient is especially decisive in the case of loading steel and concrete separately. Then, the difference between the percentages of load absorbed by each component has to be transferred by tangential forces of the interface; on the contrary, shear connectors are needed on the internal surface of the tube. As it is proposed in the Eurocodes, the limit of tangential stresses which are admitted on the interface is different for rectangular tubes than for circular sections [as it is shown in Table IV.6], owing to the evident difference in confinement effect [see Section 2.3]. As higher is the pressure on the core, higher are the tangential stresses transferred by the interface.

**Table IV.6.** Maximum  $\tau$  proposed by EC-4\*

Section	Max $\tau$
Rectangular	0.40
Circular	0.55

\* All the values are expressed in N/mm<sup>2</sup>.

Although tangential contact has been also considered in the model by means of a constant friction coefficient, the fact of loading both components simultaneously does not imply almost influence of these forces on results.

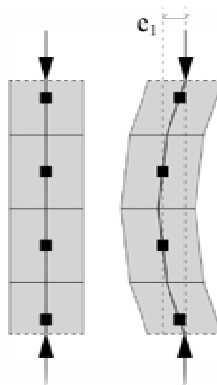
#### 4.5 Calibration of geometrical features of the models.

##### 4.5.1 Calibration of the mesh size.

Mesh size is a decisive variable to be calibrated in order to obtain the most accurate results as possible. A coarse discretization of the mesh, especially in case of the tube, leads directly to quite wrong or inappropriate results due to the geometrical nonlinearities involved in the problem. The slenderness of the plates implies bending in double curvature, and also local buckling effects.

The curvature of the plates generates important stress variations across the wall-thickness, a factor which has to be seriously considered. This is the reason why element type C3D8, with no reduced integration, has been used in the analysis, and why the analogous element C3D8R [with one unique integration point] has been discarded. The fact of using a brick element with reduced integration optimizes the time of process, but implies at the same time to obviate stress variations across the wall-thickness of the plate.

The use of reduced integration does not allow stress variations across the plate thickness, owing to have one integration point only; this fact can lead to false or inaccurate results easily, although it reduces considerably the time of process and simplifies the convergence of the problem. As it is shown in figure IV.40, the reduced integration consists in replacing each element by one integration point only, and this makes the resolution of nonlinearities much more simple, similar to the case of a compressed slender bar with initial eccentricity. However, this assumption results too much simple to reproduce problems involving important geometrical nonlinearities, since it can lead to an excess of distortion or false “buckling” of the plates due to the system becomes really sensitive to any lateral pressure.

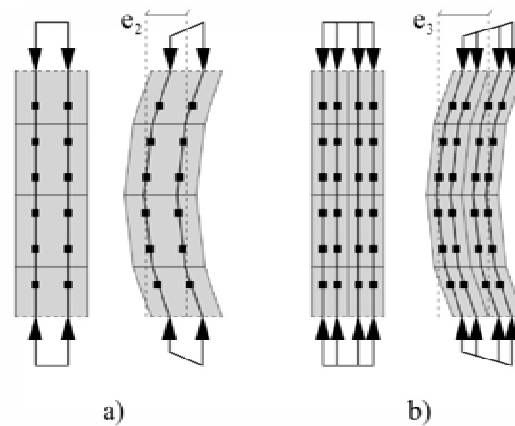


**Fig. IV.40 Undeformed and deformed shape of the plate with one-element thickness and reduced integration.**

Eccentricity may be overestimated, and this fact can lead to the distortion of the geometry.

Instead of using reduced integration, this investigation proposes the use of the solid element C3D8, fully integrated. The difference between the two elements is quite important, as the integration in the latter is done at eight different points inside each brick element. This way, the model becomes much more sensitive to the stress variations across the thickness, and the appearance of buckling is

also much more justified. Even if the discretization is really finer [with two or more elements across the wall-thickness] the analysis becomes much more accurate, (Kim, et al., 2007).

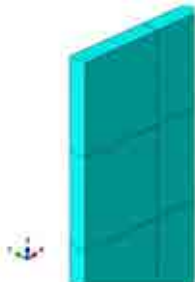
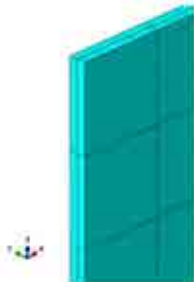

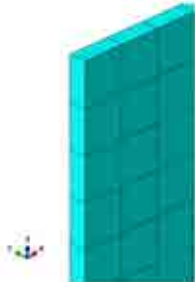




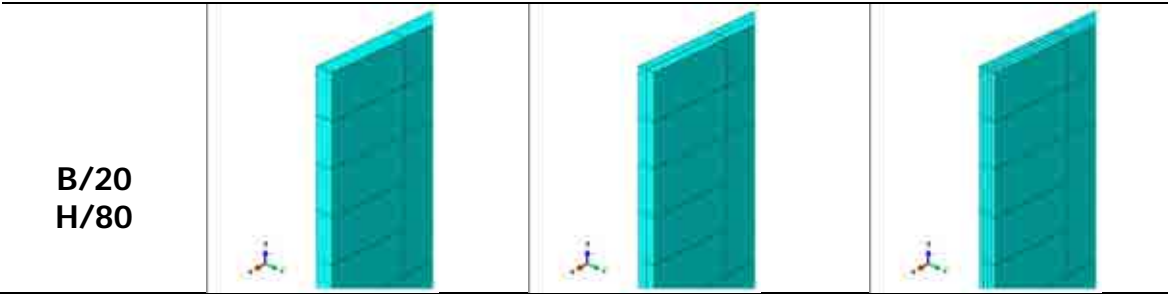
**Fig. IV.41 Idealized wall-thickness of the plates, modeled with one and two elements.**

Both models do not consider reduced integration, avoiding distortion this way.

Although a finer mesh implies less distortion, it requires more processing capabilities too. The objective of the calibration process presented below is to find the optimal proportion and number of elements in order to reproduce the plate behavior. With this aim, a set of nine analyses have been carried out, by using a slender plate of 200x500x1mm, with different mesh sizes. The influence of dividing the plate thickness into one, two or four elements and the influence of the mesh shape and size on results have been analyzed. To have an idea of the behavior of each solution beyond the maximum load-bearing capacity, the mode of buckling of each case has been compared to the theoretical one, strictly in the elastic range.

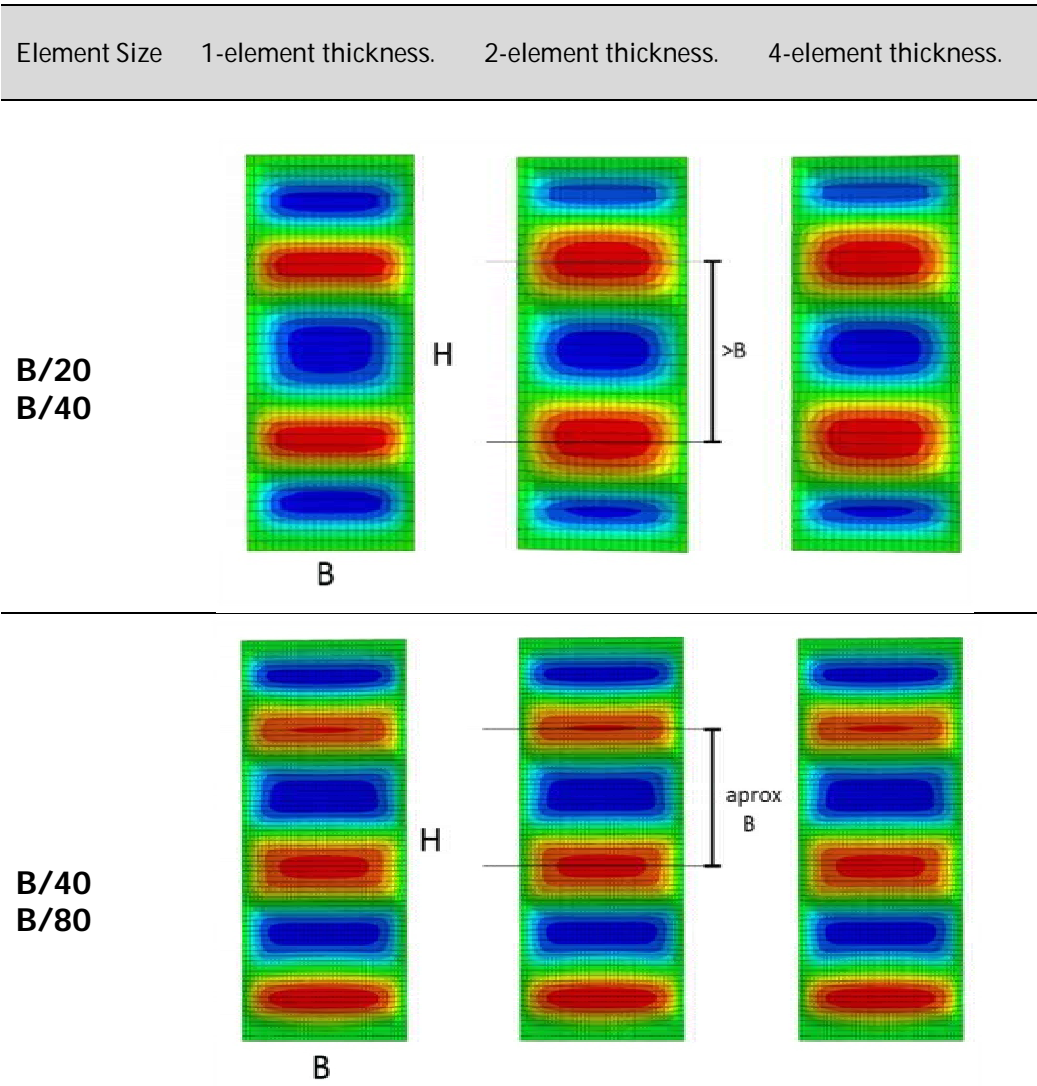
The different cases considered are the following:

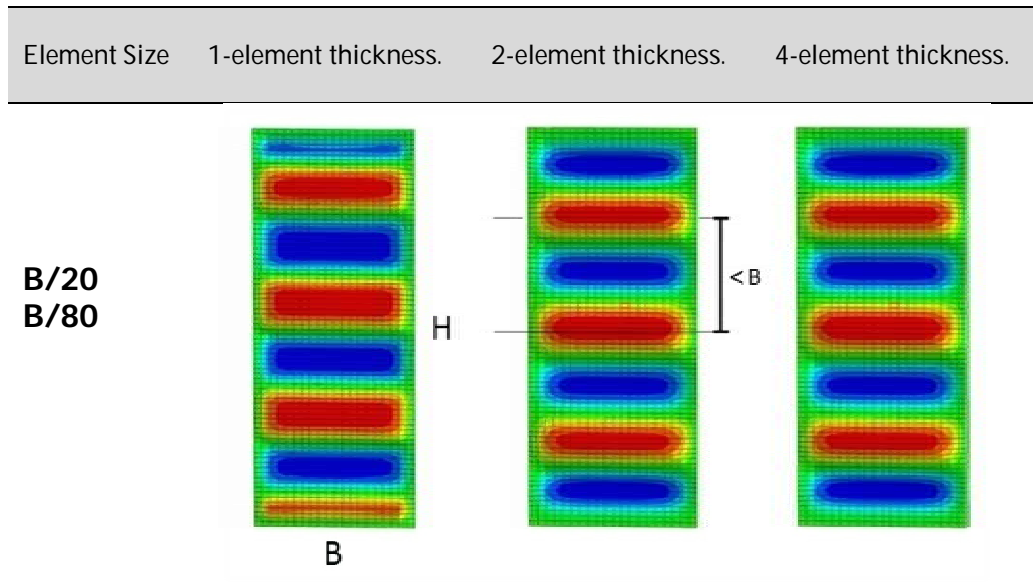
Element Size	One-element thickness	Two-element thickness.	Four-element thickness.
<b>B/20 H/40</b>			
<b>B/40 H/80</b>			



**Fig. IV.42 Different mesh sizes and proportions which have been calibrated.**  
The columns indicate the number of elements, and the rows, the proportion of the elements.

The corresponding deformed shapes, obtained from a buckling analysis, take the forms shown in figure IV.43, with some light differences related with the half wavelengths. This buckling analysis has been done by combining a uniform axial load with an insignificant distributed lateral pressure.





**Fig. IV.43 Deformed shapes obtained from a buckling analysis.**

The proportion which matches with theory more accurately, is  $B/40$  by  $B/80$ .

Note that, according to the Theory of Classical Elasticity<sup>30</sup>, the elastic half wavelength of a rectangular plate clamped in the two loaded edges and restricted against rotation in the other two, tends to be similar to the shortest edge. Thus, a buckling analysis of the mentioned thin plate in the elastic range should lead to a sinusoidal deformed shape with a value of the half wavelength close to  $B$  [200mm in this case]. A larger or shorter value of the wavelength may be caused by a slight distortion of the mesh. The buckling analysis has been done by applying an axial distributed load on two of the edges of the plate, and a minimal uniform distributed pressure on one of the lateral faces.

In figure IV.43, the results obtained from considering different mesh sizes and proportions are shown. Note that for the first row corresponding to elements of  $[B/20]$  by  $[H/40]$  size, the value of the half wavelength is larger than the shorter edge of the plate. On the contrary, the second row corresponding to elements of  $[B/40]$  by  $[H/80]$  size, gives values of the half wavelength much closer to the plate width. The third case corresponding to a rectangular shape formed by elements of  $[B/20]$  by  $[H/80]$  size tends to reduce the length of the wave owing to geometry, more dense in the vertical axis than in the horizontal one. Besides, in figure IV.42 it is shown how the discretization of the wall thickness into 1, 2 or 4 elements is also decisive in order to reflect the geometrical nonlinearities, as it has been explained before.

To determine how important the influence of the mesh size and the reduced integration is, two different analyses are presented below for the same specimen 4LN<sup>31</sup>, with the same boundary and loading conditions. While in the left case of figure IV.44 [a], the element size corresponds to a  $[B/20]$  by  $[H/40]$  element size, in the right case, it is  $[B/40]$  by  $[H/80]$ . Besides, only one element is considered in the wall-thickness in the first case, while four different elements are assumed in the latter. Needless to point out that differences in behavior are explicit, especially knowing that the  $B/t$  ratio for this section is about 37.50, and buckling effects should not appear. Thus, the deformed shape in case [b] is much more approximated to reality than the shape of case [a], assuming that only the lower face is embedded. This is a clear effect of distortion of the elements, owing to a

<sup>30</sup> See Section 3.3.2.1

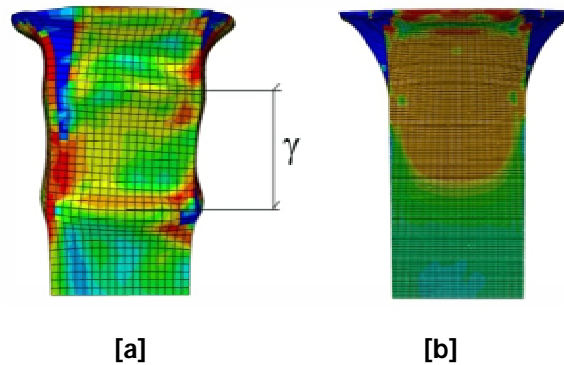
<sup>31</sup> This is a square-shaped specimen, analyzed by (Susanta, et al., 2000), and defined in Table V.7.

coarse meshing size: under this assumption, a thick-walled plate behaves as thin-walled, providing a false lecture of its axial response:

**Table IV.7.** General features of specimen 4LN, (Susanta, et al., 2000).

Section	D*	t*	D/t	fy**	fc**	fy/fc
4LN	150.00	4.00	37.50	279.9	18.1	15.46

\* All values expressed in mm\* and N/mm<sup>2</sup>\*\*



**Fig. IV.44 Different deformed shapes of the tube, depending on different meshes.**

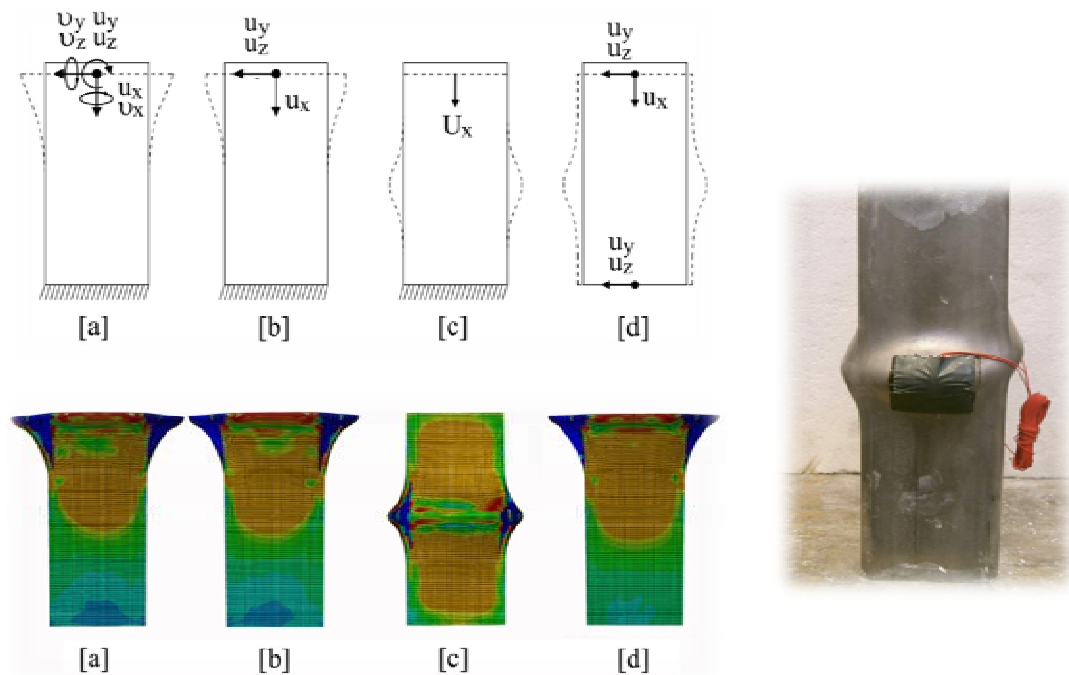
[a] One single element of  $[B/20]$  by  $[H/40]$  size in the wall-thickness.

[b] 4 different elements of  $[B/40]$  by  $[H/80]$  size in the wall-thickness.

Therefore, a combination of 3 elements in the wall-thickness of  $[B/40]$  by  $[H/80]$  size has been adopted in the whole analysis, assuming that this proposal is enough fine to guarantee the veracity of results. In conclusion, it is obvious that the element size has a clear influence on results, but this is not the unique decisive factor; boundary conditions and the domain of the model may also have a significant influence on the magnitude of the output data.

#### 4.5.2 Calibration of boundary conditions.

Boundary conditions which have been considered in the analysis are also decisive in order to obtain the closest results as possible to experimental tests. The fact of using isolated samples as a part of theoretical infinite columns implies to consider boundary conditions really seriously. It is very different to analyze a specimen pinned at the two extreme faces, than doing the same analysis by considering this specimen completely embedded. In order to validate the model used for the rest of the analyses, four different cases have been compared with different boundary conditions [Figure IV.45]. On the one hand, the first two have been defined restricted against rotation and displacement at the base: one of them with the upper face completely free [a], and the other one with its upper face restricted against rotation only [b]. On the other hand, in the other two cases, the two extreme faces have been restricted against rotation [d], by adding the restriction of displacement also in case [c].

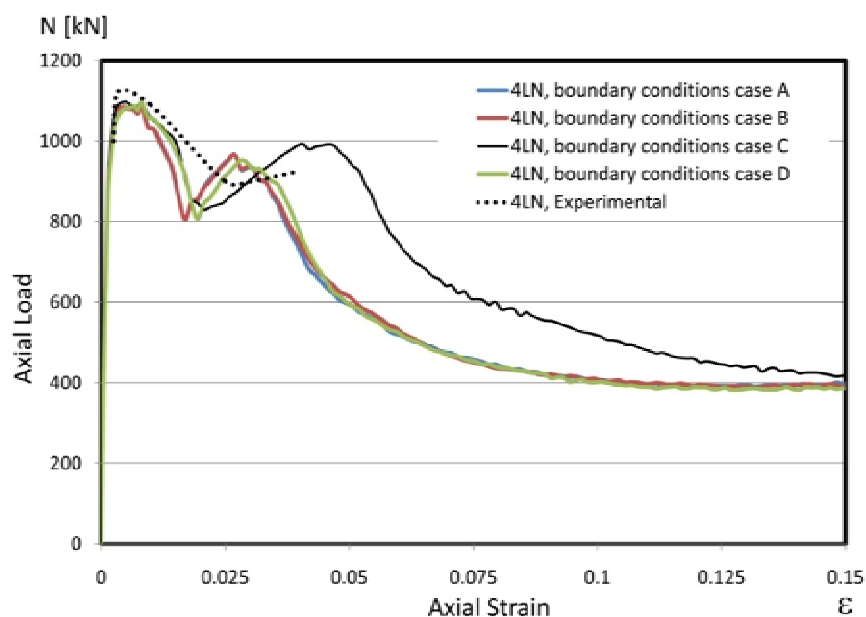


**Fig. IV.45 Different deformed shapes of the tube, according to different boundary conditions**

The rotations and displacements shown are those permitted by the different models.

The image on the right part of the figure comes from a real experiment, where the two outer faces are supposed completely embedded.

Needless to say that the case which more accurately fits with available experiments is case [c], since under compression tests, the two loading edges become almost embedded owing to friction forces. Boundary conditions are not only important to match with the existing tests, but they are also important to predict the mode of failure of the samples. Results from the four different loading cases shown in figure IV.46 [by using the same specimen 4LN, mentioned in the previous Section] are presented in diagrams of figure IV.46:



**Fig. IV.46 Axial load-strain curves corresponding to different cases of Fig. IV.45 for 4LN.**

The curve which matches more accurately with the experimental test is that of case C.

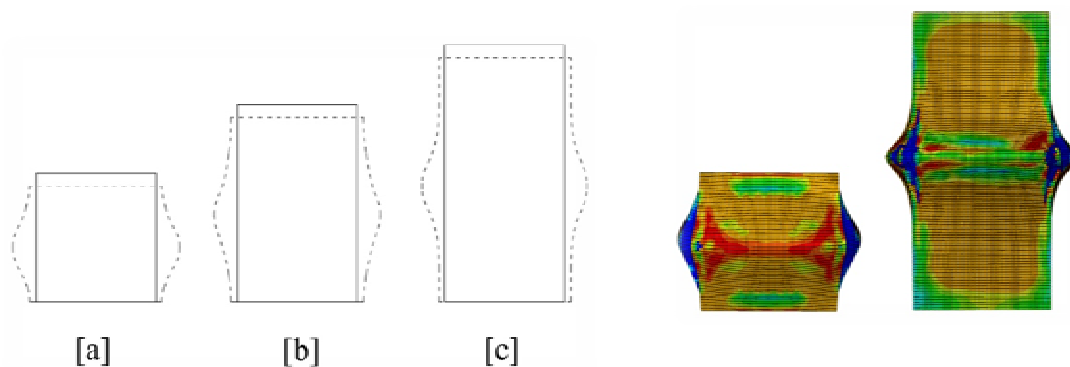
From the curves derived of the four different analyses, it is obvious that the fact of considering the specimens completely embedded in their two bases clearly enhances the ductility of the section. These conditions and their corresponding results are closer to the experimental tests made in laboratory than to the real behavior of a continuum column as a part of a whole structure. However, case [c] has been chosen for all the cases analyzed this investigation, since results have been compared to real experimental tests made with short specimens.

#### 4.5.3 Calibration of the domain of the model.

The domain of the model refers to those limits adopted in the model, in order to represent the whole reality through a reduced part of it. The simplification must reflect the entire complexity of the problem and it should not have influence on results.

##### 4.5.3.1 Calibration of the size of the specimen.

Assuming that the portion of reality which has to be simulated is a theoretical part of an infinite column, the first step in deciding the domain of the model is to choose the global size of the sample. Obviously, this election is conditioned by boundary conditions. For the case [c] adopted in the previous Section, the size of the sample must be at least two times the width of the section.



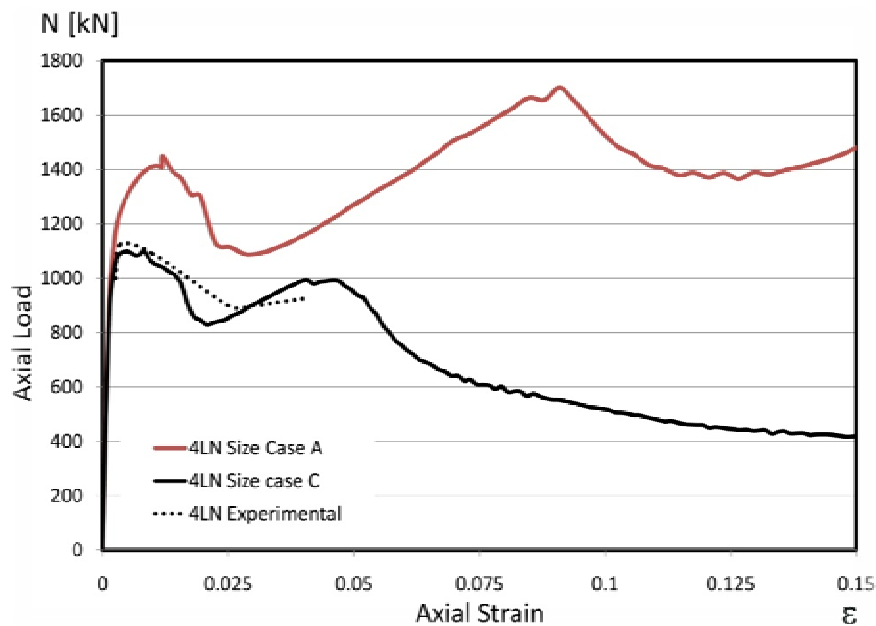
**Fig. IV.47 Different sizes analyzed of specimen 4LN.**

A height equal to the width [a], one time and half the width [b] and two times the width [c].

Knowing that a large deformation axial loading analysis goes beyond the collapse of the sample and that one of its purposes is to describe the mode of failure, the size of the tested specimen should be as large as possible. The simplification of the column into a short sample, with a height equivalent to the width, leads to an excessive gain of strength, as it can be seen in figure IV.48. The fact of having the two embedded faces really close to the failure plane in case [a] leads to overestimate the final compressive strength and the ductility of the specimen.

Therefore, and derived from the curves shown in figure IV.48, the global size which has been adopted for specimens in this investigation corresponds to a height equivalent to two times the width of the cross-section. This way, a representative portion of the column is included in the analysis, and restrictions applied to the bases should not affect the deformed shape in the failure plane.



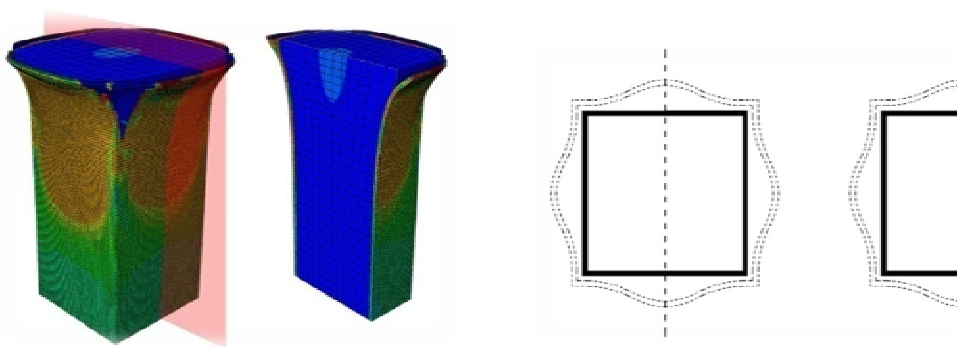


**Fig. IV.48 Comparison between the curves obtained from different sizes of the specimen.**

Cases [a] and [c] from figure IV.47 of specimen 4LN, are compared in the previous figure.

#### 4.5.3.2 Calibration of the symmetry condition.

The other geometrical parameter which determines the domain of the model is the condition of symmetry. Sections proposed in this work show a clear condition of theoretical symmetry in the two axes, "y" and "z", strictly due to geometry. This fact allows carrying out the analysis by using only half part of the model, provided that symmetry conditions were defined in the common plane.

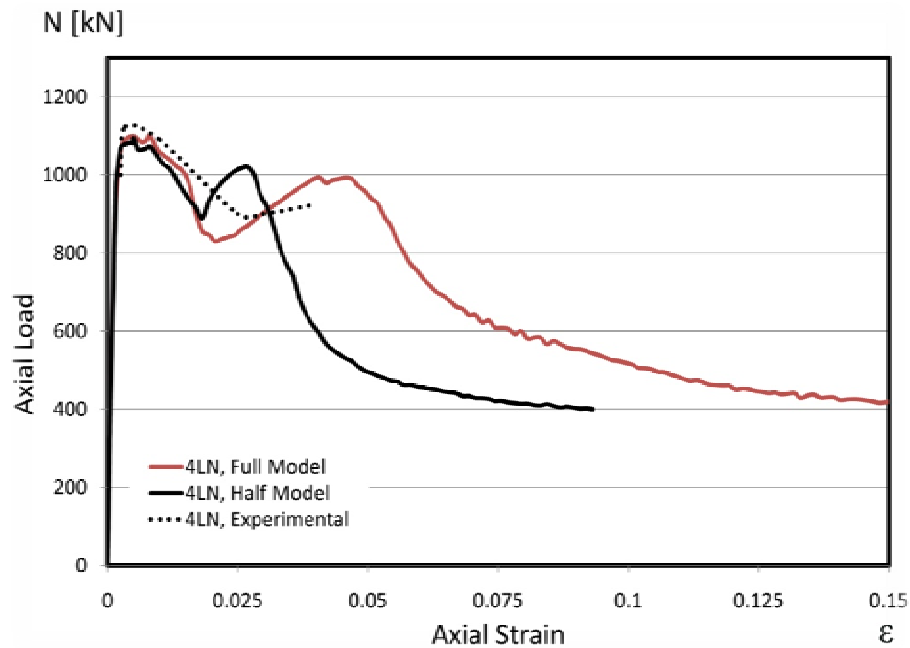


**Fig. IV.49 Condition of symmetry of the sections proposed, case of specimen 4LN.**

All sections analyzed in this investigation do show symmetry condition in the cross-sectional plane.

However, although this assumption would work perfectly well in order to determine the peak of load of the composite section, it does not represent the plastic hardening behavior and the collapse faithfully. This phenomenon is mainly due to the essence of the explicit analysis. As it can be seen in figure IV.50, the fact of considering a symmetric plane coinciding with one axis of the section reduces considerably the ductility of the whole section. Then, the fact of reducing the domain of the

model through the existing condition of symmetry would be useful for short deformation analyses, but not for large deformation axial loading.



**Fig. IV.51 Influence of the symmetry condition on the stress-strain curve.**

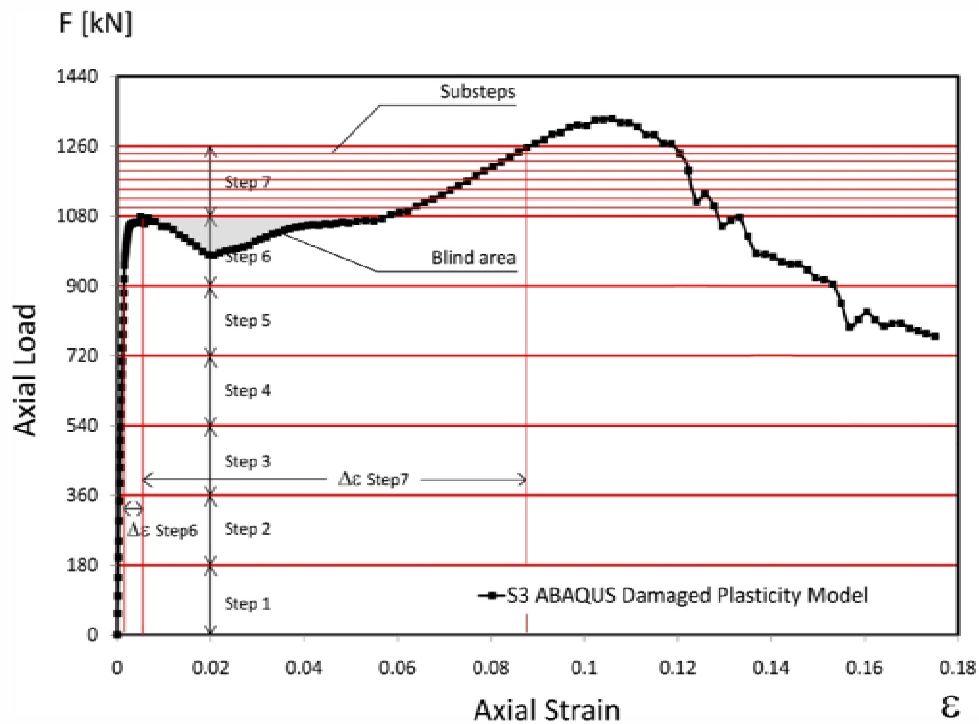
Comparison of curves obtained for specimen 4LN.

#### 4.5.4 Calibration of the loading conditions.

In general, this analysis is characterized for being materially and geometrically non linear; this is the reason why the load must be divided into different steps, according to an amplitude. This step fragmentation is decisive to solve the problem and to achieve the convergence of the solution, in models involving plasticity and buckling.

As the analyses done in this investigation imply large deformation axial loading, most part of the obtained results belong to the plastic hardening period, where small loading increments correspond to large deformation increments. Besides, it is important to take into account that this analysis aims to achieve the final collapse of the samples, and this is the reason why the descending branch after the peak of load must be also considered; the presence of a softening period implies considering also the possibility of a decent of the load-strain curve. This requirement of sensibility in front of small deformations implies a slower stepping of the load, or an extraordinary control of the process instead.

In case of loading the specimens through a distributed axial pressure applied on their upper face, the process tends to diverge when strains become important: for small load increments, vertical strains are really large [for instance,  $\Delta\epsilon$  in Step 7 of figure IV.51]. This is the reason why the load has been applied through imposed strain increments, in order to have an accurate control of the process and to simplify the convergence.

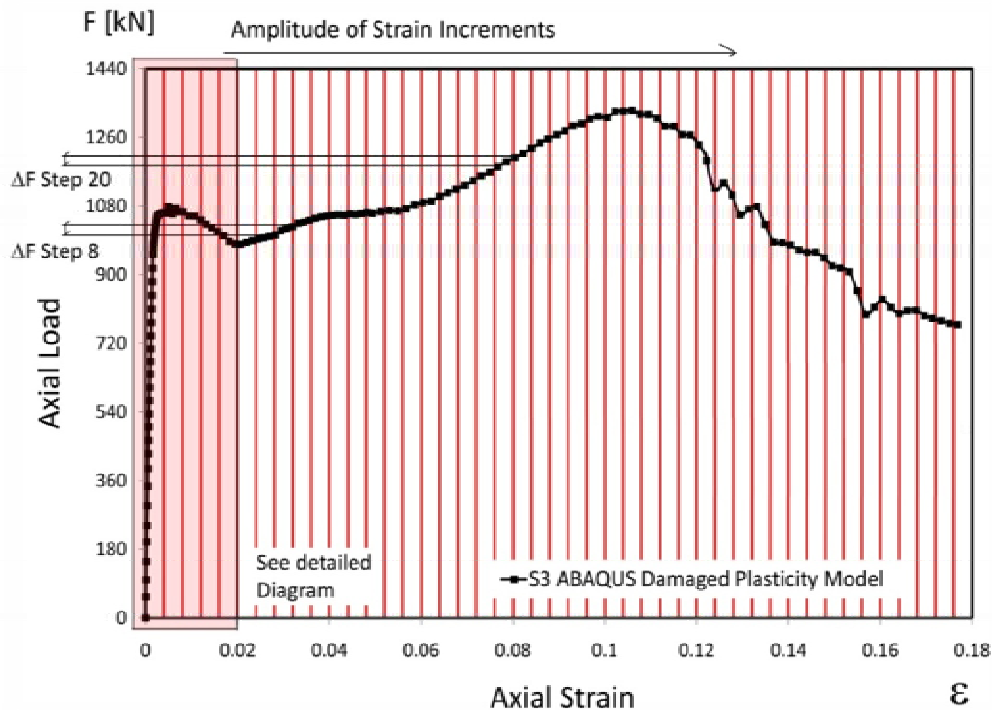


**Fig. IV.51 Definition of the loading steps by using a uniform distributed pressure.**

Due to the inversion of the predominant axis of the curve beyond the peak of load, the increment of strain in step 6 is much larger than that of the previous steps.

In case of loading through a uniform pressure at the upper face, as it is shown in figure IV.51, it is really difficult to achieve the convergence of the problem beyond the peak of load in Step 6. As it is shown in the previous figure, strain increments of steps 1 to 5 are small and almost identical; the strain increment of step 6 starts to be larger, although this fact does not distort the results; but finally, the strain increment of step 7 is much larger than the increment of step 6, and this fact leads necessarily to a lack of convergence of the problem. Besides, and owing to the descending branch after the peak of load, there is a "blind zone" of the load-strain curve very difficult to detect and control by using pressure increments only.

Thus, instead of pressure increments, all the specimens have been loaded by using increments of deformation. The concept is based on changing the reference axis of the increments, from the ordinates to the horizontal axis. This way, those results corresponding to the yield plateau [often coinciding with a descending branch] can be easily controlled, since the large axial deformation test tends to be more a horizontal curve than to a vertical diagram. Thus, equally spaced increments have been defined, by defining a specific amplitude.

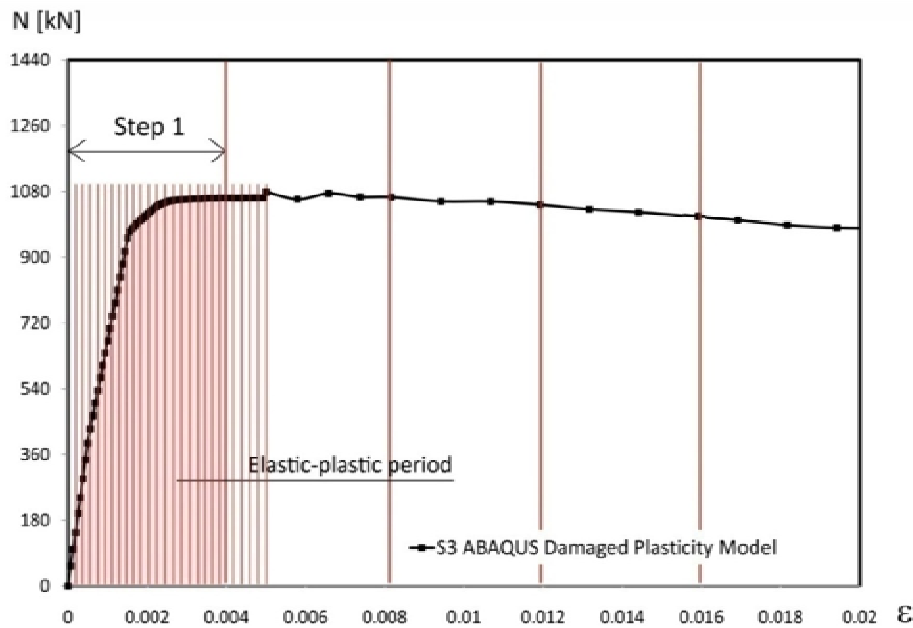


**Fig. IV.52 Definition of the loading steps by increments of imposed displacement.**

Thanks to loading the specimens by using increments of strain, the convergence of the solution is guaranteed.

Using this methodology, as it is shown in figure IV.52, main axis of the curve is the horizontal one; this way, every strain increment has its corresponding value of load, even it was negative. For instance, in figure IV.52, the load increment of Step 8 is almost identical than that of Step 20. This fact simplifies the process considerably and guarantees the convergence of the solution. However, although most part of the diagrams works really well by using strain increments, there is a reduced period in the beginning where the section behaves elastically. In the first step of figure IV.53, the increment of load is much higher than in the rest; besides, different load transferences take place between the steel and the core during this elastic phase [see Chapter V]: therefore, the description of the compressive behavior of CFT sections is impossible, if a detailed description of this first phase is neglected.

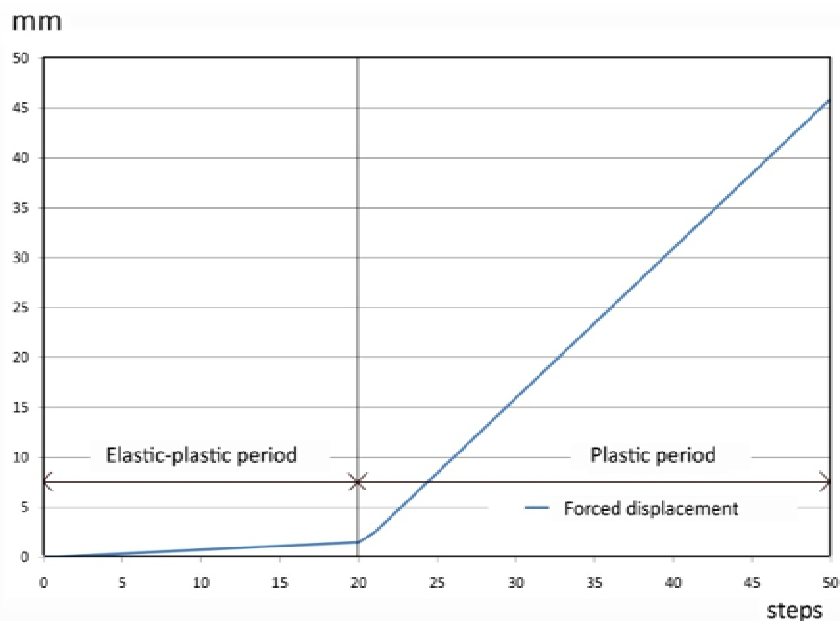
To maximize the precision of the obtained results in the elastic period, two different amplitudes of substeps have been defined, the first finer than the other. From steps one to twenty in figure IV.53, the increment of deformation is ten times finer than the rest, with the purpose of describing the volumetric expansion of concrete and the confinement of the core accurately. From step 20, the load is introduced much quickly, since the curve at this point becomes basically horizontal. This variation of the amplitude is represented in figure IV.53.



**Fig. IV.53 First part of the loading process has been divided into finer steps.**

The elastic-plastic behavior corresponding to the first period of loading of a CFT section cannot be detected by using one incremental step only.

Thus, two different linear functions have been defined in order to relate *loading steps* with displacements. This differentiation guarantees a correct density of results in all loading phases, included the first elastic-plastic period. According to Figure IV.54, up to the 20<sup>th</sup> step, a deformation of 0.10 mm per step is implemented, while from this point this strain increment grows up to a value of 1.50 mm.



**Fig. IV.54 Two linear functions have been defined for introducing the loading steps.**

The elastic-plastic period is more slowly loaded than the rest.

